

# Sub-Aperture Motion-Adaptive Reconstruction Techniques for Digital Beamforming Airborne SAR

Juan Pablo Navarro Castillo, Rolf Scheiber, Marc Jäger, and Alberto Moreira, *Fellow, IEEE*

**Abstract**—The use of airborne synthetic aperture radar (SAR) to demonstrate high-resolution wide swath (HRWS) operational modes in spaceborne SAR missions has supported the development of advanced digital beamforming (DBF) techniques. In doing so, one of the challenges to overcome is the temporal variation of the antenna phase centers in the airborne DBF SAR scenario, which significantly degrades the performance of the azimuth reconstruction. Multiple motion compensation (MoCo) solutions have been explored to correct these inconsistencies. However, the compensation of residual phase errors in the Doppler domain remains unresolved when the multi-channel data has an aliased azimuth spectrum. This paper proposes an algorithm that exploits the properties of the DBF azimuth reconstruction to correct these residual motion inconsistencies, although the channels are undersampled. The algorithm modifies the input range-compressed multi-channel data by using an innovative MoCo technique to compensate the phase components coming from undesired 3D time-variant baselines between the different apertures. Furthermore, a 2-step azimuth reconstruction configuration is implemented to account for the polychromatic nature of SAR signals. To test the performance of the algorithm, point target simulations were carried out, in which the impact of a realistic across-track motion, inaccuracies in the digital elevation model (DEM), and variable velocity are analyzed. The results confirm the efficacy of the proposed technique in azimuth ambiguity suppression, where excellent ambiguity suppression is observed after applying the proposed MoCo technique. Finally, the outcome of the simulations is validated with real multi-channel data acquired by the German Aerospace Center (DLR) airborne DBFSAR system.

**Index Terms**—digital beamforming, motion compensation, azimuth reconstruction, airborne SAR, azimuth ambiguities, velocity variation.

## I. INTRODUCTION

IN the last decades, the research related to spaceborne HRWS SAR missions has developed considerably. The desire to achieve finer resolution in azimuth while covering a wide swath has led to a new generation of systems that implement DBF to overcome the limitations of a standard monostatic stripmap SAR sensor. To get better azimuth resolutions, these systems use multiple apertures displaced along-track, which simultaneously receive radar echoes from the same area on the ground. After the SAR data acquisition, the information stored in each receiver, or channel, is processed by a bank of filters, called reconstruction filters. These systems are expected to have an aliased multi-channel Doppler spectrum because the pulse repetition frequency (PRF) has to

The authors are with the Microwaves and Radar Institute, German Aerospace Center (DLR), 82234 Weßling, Germany (e-mail: Juan.NavarroCastillo@dlr.de).

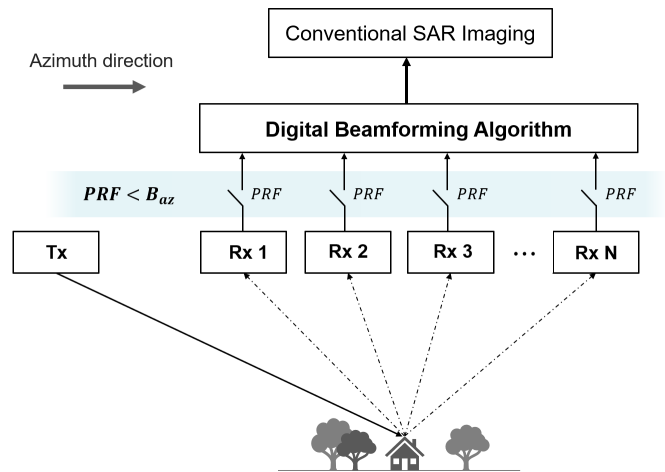


Fig. 1. Block diagram of a multi-aperture SAR system using azimuth DBF on receive. A transmitter sends a pulse and the echoes of all illuminated targets are stored in multiple receivers displaced along the azimuth direction. The PRF of each receptor is smaller than the acquired azimuth bandwidth ( $B_{az}$ ), resulting in an aliased azimuth spectrum. The 2D information of the receivers will be then processed with a certain DBF algorithm and mixed, producing an output 2D SAR signal without aliasing, which can be subsequently processed by a conventional SAR processor.

be small to, for instance, avoid range ambiguities or reduce the required average power of the transmit signal [1]. If the PRF is smaller than the Doppler bandwidth needed to achieve the intended azimuth resolution, azimuth ambiguities will appear in the image. Fig. 1 illustrates the DBF on receive principle.

This paper is organized as follows. Section II introduces the airborne SAR system used for this work and an example of real motion irregularities that deteriorate the performance of a traditional reconstruction algorithm. Section III presents the proposed techniques to improve airborne DBF SAR performance by implementing motion corrections before azimuth reconstruction. Section IV analyzes the performance of the suggested reconstruction algorithm with simulations and then validates the results with a real example. Section V summarizes the main contributions and findings of this article.

### A. Azimuth Reconstruction Algorithms

Currently, there is a wide range of different approaches to define the reconstruction filters. As explained in [2], these methods can be organized into three categories: matrix inversion methods, adaptive methods, and time domain methods.

Using the generalized sampling theorem [3] Krieger et al. implemented a solution based on the filter configuration

presented in [4], proposing a matrix inversion method for the reconstruction in azimuth of non-uniform undersampled multi-channel SAR signals [5]. This approach builds the filters by solving a system of linear equations. Coherently summing the output of the aliased channels after passing the respective reconstruction filters allows the algorithm to unambiguously reconstruct the Doppler spectrum. The final result is a range-compressed SAR signal equivalent to a channel sampled with a PRF  $N$  times greater than the original [5], where  $N$  denotes the number of channels used in the algorithm. These linear equations are based on the multi-channel SAR impulse response function (IRF).

Starting from this point, some variations of this method have been proposed. First, [6] proposed a polychromatic reconstruction where the filters are defined in the wavenumber domain, in contrast to [5] where the filters are defined in the range-Doppler domain. However, none of these solutions could account for all the phase errors introduced by their respective assumptions in the case of large along-track distances between different receiver phase centers. In the case of [5], neglecting the polychromatic nature of SAR signals and the corresponding change of the Doppler rate in the reconstruction led to non-negligible phase errors and a considerable increase of the azimuth ambiguity-to-signal ratio (AASR). Similarly, ignoring the variation of the bistatic IRF over range, as in [6], also results in a degradation of the AASR. Then, Sakar et al. presented an innovative solution for multi-static systems with larger baselines by using a two-step reconstruction to overcome these limitations [7], [8].

In the last years, several authors have presented different variations of the matrix inversion method to mitigate its limitations when strong non-uniformity or coinciding samples in azimuth are expected in the system. Works like [9] and [10] modified the original block structure, and implemented a cascaded network aiming to reduce the impact of noise scaling because of non-uniformity. Other solutions define a way to filter out the unnecessary redundant information by redefining the matrix inversion method as a least squares (LS) problem, improving the noise scaling at the expense of resolution loss [2], [11], [12].

The second family of reconstruction algorithms, referred to in [2] as adaptive methods, aims to minimize the undesired combined power of both azimuth ambiguities and white noise, requiring an accurate estimation of the ratio between noise and ambiguous power [1]. This fact makes these approaches data-dependent, in contrast to matrix inversion methods. The first solution using this principle was the space-time adaptive processing (STAP) technique [13], which did not show a good performance in terms of ambiguity suppression for HRWS systems [14]. In [15], the authors modified STAP by implementing a linearly constrained minimum variance algorithm based on a multi-Doppler-direction restriction, where nulls are formed for Doppler ambiguity directions, showing better results in terms of AASR. A variation was proposed in [16], which is based on imaging STAP (ISTAP) and aims to maximize the signal-ambiguity-plus-noise ratio (SANR). The authors in [14] presented an algorithm that uses a generalized minimum mean-square error (MMSE) cost function to create

a flexible method that includes a weighting factor to prioritize either ambiguity suppression or noise scaling reduction. Further adaptive reconstruction methods to optimize the trade-off between ambiguity suppression and noise level can be found in [17], which also includes a comparison of some existing reconstruction algorithms.

Finally, the last group of reconstruction algorithms performs DBF in the time domain. Originally, the first solution proposed for HRWS systems were filters that just interleaved the samples of the different channels to obtain an image that could theoretically achieve higher resolutions [18]. However, as discussed in [9] and [14] this solution can only be used when the multi-channel azimuth sampling can be considered to be uniform since the AASR increases dramatically as soon as the chosen PRF leads to a non-uniform configuration. In addition, interleaving algorithms do not take into account relative differences between channels like non-identical antenna patterns or irregular motion. In [19], several back-projection reconstruction algorithms are introduced and compared. These algorithms have considerable potential but are anticipated to demand significant computational resources compared to frequency domain approaches. Consequently, it was decided not to further investigate these types of algorithms. Recently, [20] presented an innovative reconstruction defined in the time domain. In this case, the authors combine a variable PRI scheme, analogous to the one used in staggered SAR [21], together with a polychromatic time domain reconstruction algorithm that uses a Wiener filter to compute the reconstruction weights. This solution aimed to reduce the impact of noise scaling due to sampling singularities in multi-static SAR constellations.

In the work presented in this paper, the reconstruction algorithm is based on a matrix inversion method. As such, the proposed approach is data-independent, computationally efficient, and relatively easy to implement [11]. As the chosen sampling is nearly uniform, noise scaling is not expected to be critical for the system used in the experiments presented in this paper. Therefore, the use of an adaptive method or the time domain method presented in [20] to reduce the impact of noise scaling was not necessary.

## B. MoCo Techniques

HRWS systems are primarily of interest in spaceborne missions but they need to be validated with airborne demonstrations [22]–[26]. However, in airborne SAR, turbulence, vibration, and other undesired factors introduce motion inconsistencies that degrade the SAR image's focusing performance and the reconstruction performance [27]. Several MoCo algorithms have been proposed to correct these effects [28].

One well-known method is the two-step MoCo (TS-MoCo), presented in [29], [30]. The first step consists of a phase and envelope correction for a reference range, commonly set in the center of the swath. Then a second range-dependent residual correction step is performed. However, the corrections are only applied to the center of the beam. In [31], an analysis of this approximation is provided. Another restriction of this algorithm is the fact that a constant reference height is assumed for

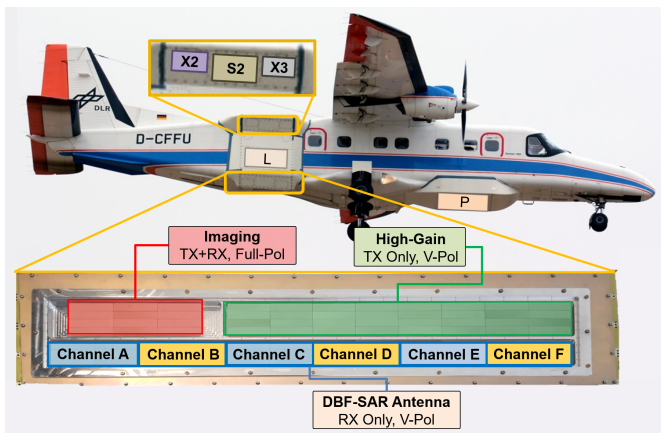


Fig. 2. DBF antenna array in the DLR DO 228-212 aircraft operating in the X-band. The Rx channels colored in yellow are the ones used in the experiments presented in this paper. The F-SAR X2 antenna was used as a transmitter.

the whole scene. New MoCo approaches were proposed, which overcome these limitations by correcting the residual aperture-dependent phase error and using a DEM to adjust the height to a more realistic scenario. These methods, also known as topography- and aperture-dependent (TA) MoCo algorithms, are compared and analyzed in [32]. They can be subdivided into three groups: precise TA (PTA) [33], sub-aperture TA (SATA) [34], and frequency division (FD) [35]. More recent studies [36]–[38] have analyzed and proposed new potential improvements for TA MoCo methods, but they will not be further described in this document. Other investigations like [15] and [27] have studied the additional phase errors of each channel due to, for instance, aperture position errors and how to estimate and correct them. Additionally, in [27] the authors presented a DBF algorithm where the individual channel errors are corrected first using a one-step MoCo, based on the proposal presented in [39], and an aperture-dependent MoCo. However, none of these approaches is equipped to accurately compensate motion for a multi-channel system, where the individual channels have an aliased spectrum in azimuth when the PRF is lower than the acquired azimuth bandwidth, which is normally the case in azimuth DBF on receive.

### C. Contributions

The algorithm proposed in this paper introduces a MoCo step within the reconstruction filtering process to allow for fully Doppler-dependent compensation of residual inter-channel motion even when receive channel spectra are aliased in azimuth. In addition, the proposed technique will not assume a global linear reference track, but two non-linear tracks, one for transmission (Tx) and one for reception (Rx). Furthermore, this technique does not impose constraints regarding imaging geometry, e.g. it could be applied to non-linear acquisitions such as circular SAR. The objective is to minimize the channel phase corrections in the reconstruction. Then the major MoCo corrections will take place after signal reconstruction, now applying an approach based on the state-

of-the-art techniques described above, where a reference linear track is used.

This work will apply a similar reconstruction approach as presented in [5], but with four main differences. First, as will be described in Section III the MoCo algorithm will transform a semi-active multi-channel configuration with one transmitter into a fully-active constellation with  $N$  virtual transmitters, where  $N$  is the number of receivers. Secondly, a new range-dependent component will be defined in the reconstruction filters to implement a residual Doppler MoCo correction, as mentioned before. Thirdly, a two-step reconstruction scheme similar to the one introduced in [8] will be used. The fourth and last change is related to the selection of the reference track, where normally the monostatic track of the transmitter is chosen. In this case, the output reference track will be bistatic and composed of the original trajectory for Tx and an arbitrarily chosen track among the trajectories for Rx.

## II. DLR DBFSAR AIRBORNE SAR: SYSTEM CHARACTERISTICS

In this section, the current DLR DBFSAR airborne antenna configuration will be briefly presented. Additionally, the motion irregularities of the system will be illustrated using a real example. Finally, the implications of these motion inconsistencies on the definition of the multi-channel SAR IRF are briefly discussed.

### A. Multi-Channel Airborne Antenna Array

For the demonstration of the techniques presented in this investigation, the DLR DBFSAR airborne system was used. This system is set to succeed of the original DLR F-SAR airborne system [40]. Some of the antennas used in F-SAR were substituted with a new set of antennas for DBF experiments. The antenna distribution of the DBFSAR airborne system is depicted in Fig. 2. The DLR DBFSAR presently supports simultaneous data acquisition in X and L bands. Although for the present paper only the X-band subsystem is of interest. The DBFSAR receive antenna configuration in the lower part of Fig. 2 is the basis for the implementation of more advanced techniques such as DBF and multi-channel ground and marine moving target indication (MTI). The F-SAR antenna X2 was set as the transmitter for the DBF system and three of the sub-arrays in the Rx-only DBFSAR antenna as receivers. The separation in the flight direction between two consecutive DBF Rx antennas is approximately 20 cm. Each antenna comprises several DBF-receive antenna modules (DBFRAM). More technical details about the antennas can be found in [40] and [41].

In Fig. 2 the Rx channels associated with the sub-arrays colored in yellow (B, D, and F) are the ones used throughout this study. For the sake of simplicity, the bistatic channels composed of X2 as transmitter and the Rx-only sub-arrays "B", "D" and "F" as receivers will be referred to as bistatic channels 1, 2, and 3, respectively, for the rest of the discussion. It is important to remark that parameters such as system delays, antenna pointing and phase center position, as well as relative channel phase offsets have been calibrated based

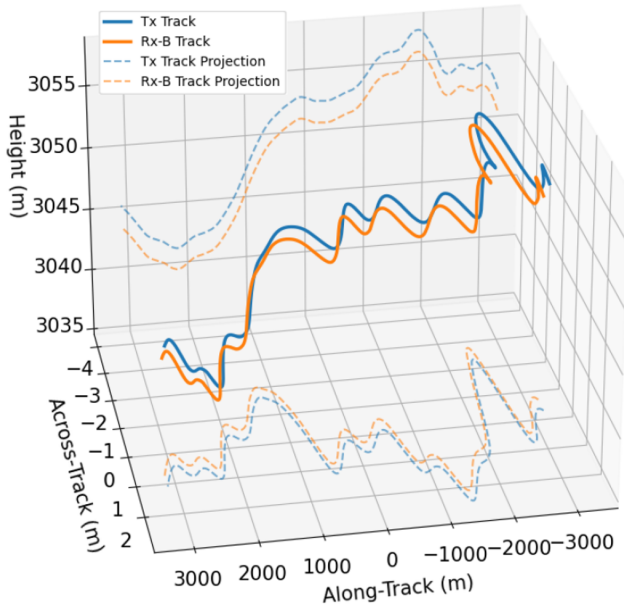


Fig. 3. The trajectory of the Tx (continuous blue line) and Rx (continuous orange line) apertures in the bistatic channel 1, introduced in Section II-A. The dashed lines represent their respective projections in the along-track/across-track plane (behind the 3D track) and the along-track/elevation plane (below the 3D track).

on the approach presented in [42]. Therefore, no data-driven estimates of these parameters needed to be incorporated into the reconstruction process.

### B. Irregular Variation of Inter-Channel Baselines

Standard azimuth reconstruction algorithms suppose ideal linear tracks and constant baselines between the channels. This is clearly not the case for airborne platforms, where the tracks are non-linear and the baselines between the channels vary due to translational and rotational motions inherent to airborne systems. Neglecting to compensate for this irregular motion in a DBF airborne SAR system will lead to a bad performance in terms of ambiguity suppression, as shown in [27] and Section IV. In this section, the bistatic tracks of the DLR DBFSAR airborne system and the channel baselines will be shortly analyzed. The study will be focused on the bistatic channels 1, 2, and 3, presented in Section II-A.

An example of a real bistatic track from a test campaign carried out in October 2020 is shown in Fig. 3. The trajectories of the apertures were measured by the DLR DBFSAR navigation system. This measurement is carried out using differential GPS techniques and the absolute position is typically accurate in the centimeter range. Since the absolute position error is the same for all antenna phase centers, the baselines are not affected by it. The image corresponds to the bistatic channel 1, where the transmitter (blue line) is the F-SAR antenna X2 and the receiver (orange line) is the DBF Rx-only channel B. Looking at their projections reveals that the trajectories are non-linear and that there is a relatively large baseline of close to 2 m between Tx and Rx. To analyze the irregular motion more in-depth, Fig. 4 provides the baselines between the transmitter

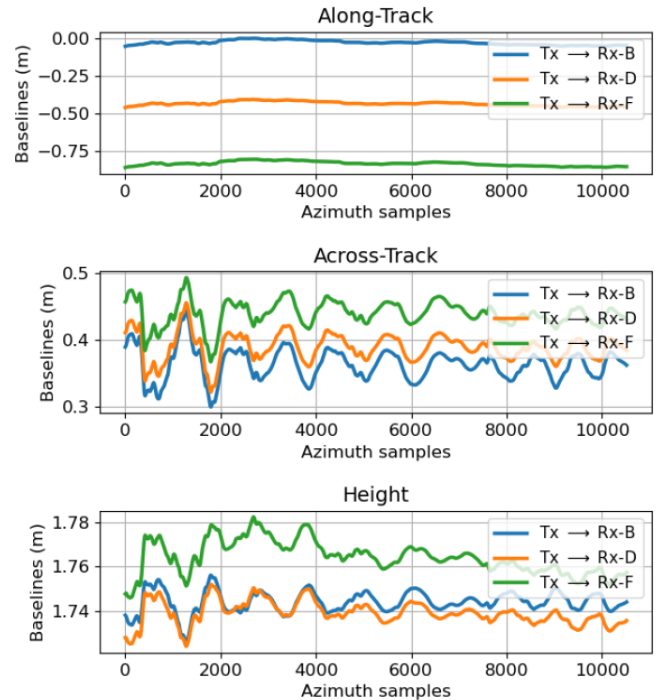


Fig. 4. Time-variant bistatic baselines between the Tx (X2 antenna) and the Rx-only channels B, D, and F in the DLR DBFSAR airborne system.

X2 and the receivers B, D, and F, respectively, in the three dimensions of Fig. 3. The along-track axis in this example is set to be approximately parallel to the flight direction. As suggested by Fig. 2, there is a big baseline in elevation/height between the receivers and the transmitter. The inter-channel separation in along-track corresponds to approximately 40 cm. The relative baselines in the coming sections are defined as the difference between the baselines of the bistatic channel 1 (blue lines in Fig. 4) and the other two bistatic channels (orange and green lines in Fig. 4).

It is important to note that the algorithm presented in the following sections incorporates the use of azimuth blocks, where the flight direction is updated in each block. This means that the along-track axis will vary from block to block. However, to simplify the introduction of the system characteristics, the along-track axis is assumed to be fixed in time throughout Section II.

Supposing an arbitrary Cartesian coordinate system, the position of an aperture with index  $\psi$  can be expressed as

$$q_{\psi}(t) = \begin{bmatrix} x_{\psi}(t) \\ y_{\psi}(t) \\ z_{\psi}(t) \end{bmatrix} \quad (1)$$

where  $t$  denotes the slow time variable. Then, the baseline between the transmitter ( $\psi = Tx$ ) and a receiver  $i$  ( $\psi = Rx_i$ ) can be defined as

$$b_{Rx_i \rightarrow Tx}(t) = q_{Rx_i}(t) - q_{Tx}(t). \quad (2)$$

Generally, knowing the baselines between the transmitter and the different receivers and setting one of the bistatic channels as reference (channel 1 for instance), the relative baseline of an arbitrary semi-active bistatic channel  $i$  is

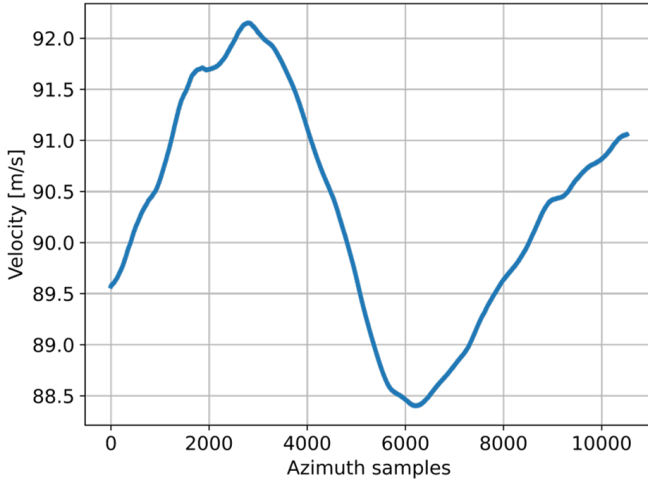


Fig. 5. Real velocity variation of a real flight using the DLR DBFSAR airborne system corresponding to the Tx aperture. The average velocity was 90.11 m/s.

$$\Delta b_{R_{x_i} \rightarrow R_{x_{ref}}}(t) = \frac{q_{R_{x_i}}(t) - q_{R_{x_{ref}}}(t)}{2} \quad (3)$$

where  $\Delta b_{R_{x_i} \rightarrow R_{x_{ref}}}(t)$  expresses the time-variant relative baseline between the phase center of the bistatic track  $i$  and the phase center of the reference bistatic track in a semi-active constellation. The factor 2 accounts for the fact that the effective phase center of a bistatic track is assumed to be located halfway between transmitter and receiver.

### C. Standard Bistatic SAR IRF

The DBF filter equations used in the present approach are obtained by inverting a matrix that defines the differences between the bistatic IRF of each channel and the selected reference IRF in the range-Doppler domain, as described in [5]. The monostatic SAR IRF is usually chosen to be the reference, taking the transmitter phase center to set the baselines that are used to define the bistatic IRF for each channel. In this approximation, the bistatic IRF can be seen as a monostatic SAR IRF with a certain time delay and a constant phase offset. The sensor velocity ( $\bar{v}$ ) used in the IRF can be defined as

$$\bar{v} = \text{mean}_t(v(t)) \quad (4)$$

where

$$v(t) = [v_x(t), v_y(t), v_z(t)]. \quad (5)$$

$v(t)$  is the sensor velocity at each slow time instant and for the three directions of the Cartesian coordinate system ( $x$ ,  $y$ , and  $z$ ). Since the bistatic IRF will be defined in the range-Doppler domain, the value of the velocity cannot be introduced as a function of time, so the average of the velocity is used as an approximation of the real sensor speed. The approximation in [5] assumes that the velocity and flight altitude are constant, the apertures follow a straight path and there are no across-track offsets between the Tx and Rx antennas.

The separation in azimuth (or along-track) direction between the different apertures can be derived from the bistatic

baselines introduced above. First, the unitary vector containing the flight direction is calculated by normalizing the average velocity vector presented in (4):

$$u_{az} = \frac{\bar{v}}{\|\bar{v}\|}. \quad (6)$$

Then, the time-variant distance in azimuth between the transmitter  $T_x$  and the receiver  $R_{x_i}$  can be calculated as the projection of the bistatic baselines onto the flight direction vector:

$$d_{R_{x_i} \xrightarrow{az} T_x}(t) = b_{R_{x_i} \rightarrow T_x}(t) \cdot u_{az}^T \quad (7)$$

Also, the separations in azimuth for each bistatic channel cannot be defined as a function of time in the bistatic IRF used to construct the reconstruction filters in the Doppler domain. For this reason, the separation along-track for each bistatic channel is approximated by its mean value:

$$\bar{d}_{R_{x_i} \xrightarrow{az} T_x} = \text{mean}_t(d_{R_{x_i} \xrightarrow{az} T_x}(t)). \quad (8)$$

Finally, considering the difference between sensor speed and beam velocity on the ground to be negligible, the bistatic IRF  $H_i(f_a, r; f_r)$  of an arbitrary channel  $i$  can be expressed in the range-Doppler domain as

$$H_i(f_a, r; f_r) = M(f_a, r; f_r) \cdot \exp\left[-j \cdot \frac{\pi}{2} \cdot \frac{f_r \cdot \bar{d}_{R_{x_i} \xrightarrow{az} T_x}^2}{c_0 \cdot r}\right] \cdot \exp\left[-j \cdot 2\pi \cdot f_a \cdot \frac{\bar{d}_{R_{x_i} \xrightarrow{az} T_x}}{2\|\bar{v}\|}\right] \quad (9)$$

where  $M(f_a, r; f_r)$  is the monostatic SAR IRF defined in the range-Doppler domain. The dependency on the range frequency  $f_r$  emphasizes the polychromatic nature of SAR signals.  $r$  denotes the slant range, and  $f_a$  the unwrapped Doppler frequency  $f_a \in \left[-\frac{N \cdot PRF}{2} + f_d, \frac{N \cdot PRF}{2} + f_d\right]$ , where  $f_d$  and  $N$  denote the Doppler centroid (FDC) and the number of channels, respectively. It is important to define the frequency axis as unwrapped from the start since the reconstruction filters will be defined for this bandwidth. Nevertheless, the original channels are subsampled meaning that the Doppler bandwidth is wrapped within an interval equal to the PRF.  $c_0$  denotes the speed of light. The range-dependent exponential component denotes a relative offset in slant range between the different bistatic channels and is characteristic of semi-active configurations.

However, given that the antennas do not follow the same path and that the baselines in across-track are not zero and vary over time, this IRF approximation may deviate considerably from the real IRF. In addition, the range-dependent offset approximation in (9) does not hold for big azimuth baselines, as demonstrated in [7]. Furthermore, in (9) the velocity of the sensor is assumed to be constant, but in reality, the speed of an airborne SAR system varies over time as illustrated in Fig. 5, where the deviation from the nominal velocity for the flight presented in Fig. 3 is seen to lie in the range  $\pm 2$  m/s. Studies such as [8] have concluded that velocity variation in multi-static spaceborne DBF SAR systems can be neglected. As will be discussed in more detail in Section IV, this is not the case

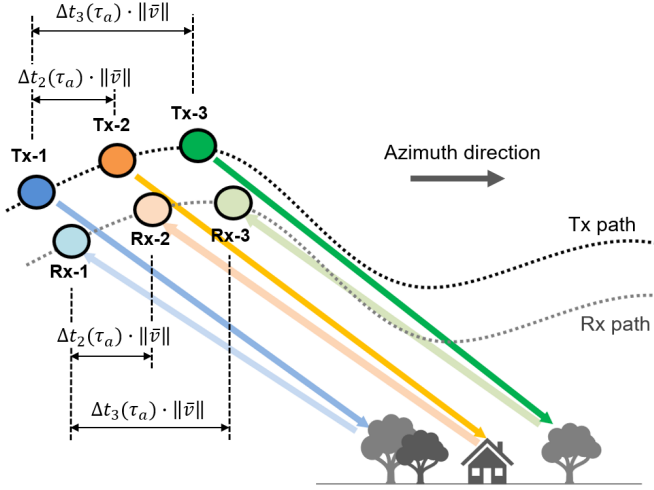


Fig. 6. fully-active DBF SAR system where Tx and Rx do not coincide in space. The time delay between the trajectories of the transmitters is the same as between receivers and varies over time. The example in this figure shows the time delays for the time instant  $t = \tau_a$ .

for airborne SAR sensors. A solution to minimize this effect is to divide the image into small azimuth blocks and process them separately to reduce the velocity and baseline variation within one block.

### III. MOTION ADAPTIVE RECONSTRUCTION ALGORITHM

Before introducing the new reconstruction algorithm, it is important to understand the system model on which the proposed solutions are based. The aim is to exploit the matrix inversion DBF algorithm principle to allow residual phase errors coming from the beam-center relative MoCo (RelMoCo) to be corrected within the reconstruction process. The idea of the RelMoCo algorithm is to redefine the multi-channel system as a fully-active multi-static constellation and do the respective transformations in each bistatic channel. The use of relative baselines allows an easier and more accurate definition of the filters and output geometry since the reference bistatic channel is kept unaltered. Working with the original non-linear trajectories reduces the magnitude of the phase corrections performed before reconstruction. This minimizes the residual errors due to the use of assumptions to define the system IRF. After the reconstruction, the remaining motion contributions coming from a non-linear trajectory can be accurately compensated using advanced MoCo techniques, which can only be applied to a dataset with a non-aliased Doppler spectrum. The proposed reconstruction algorithm will be introduced after the system model has been established.

#### A. Alternative Multi-Static System Model

The motivation to choose a fully-active configuration to redefine the semi-active bistatic IRF is to make the selection of the reconstructed output geometry more flexible. Before presenting the redefined bistatic IRF, the reference fully-active configuration used in this approach will be introduced.

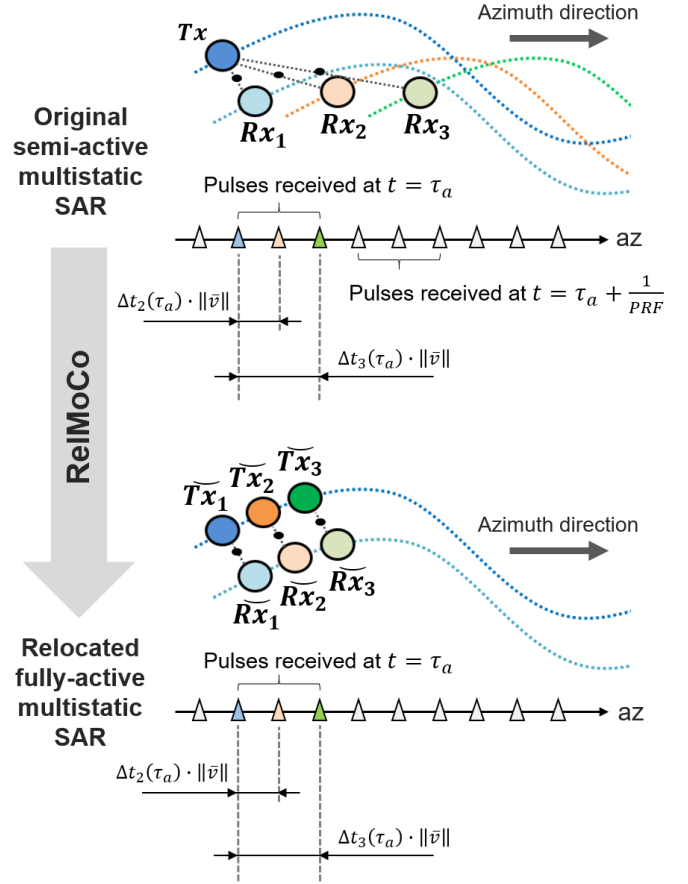


Fig. 7. Proposed transformation from a semi-active multi-static SAR formation into a fully-active multi-static SAR constellation. The black points between transmitters and receivers represent the approximated position of the phase center for each bistatic channel. In this example,  $\bar{R}x_1$  is the reference receiver. Consequently, the location of the apertures  $\bar{T}x_1$  and  $\bar{R}x_1$  is the same as the location of  $Tx$  and  $Rx_1$ , respectively.

In this ideal constellation, each bistatic channel is composed of a different transmitter and a respective receiver. Additionally, all receivers and transmitters must follow the same bistatic path. In other words, there will be a unique path for the receivers and a unique path for the transmitters. It is assumed that the time delay between the trajectories for Rx is the same as for Tx. This concept is depicted in Fig. 6. Using this approach the bistatic IRF of each bistatic channel can be defined as the IRF of one of them with just an additional time delay. Then, the bistatic IRF for an ideal fully-active constellation such as the one presented in Fig. 6 can be formulated as

$$H_i(f_a, r; f_r) = H_{ref}(f_a, r; f_r) \cdot \exp \left[ -j \cdot 2\pi \cdot f_a \cdot \bar{\Delta}t_i \right] \quad (10)$$

where

$$\bar{\Delta}t_i = \text{mean}_t(\Delta t_i(t)). \quad (11)$$

$H_{ref}(f_a, r, f_r)$  is the polychromatic bistatic IRF of the reference channel,  $\Delta t_i(t)$  is the time delay between the reference bistatic channel and the bistatic channel  $i$  and  $\bar{\Delta}t_i$  its mean value over time.

Nevertheless, real DBF SAR systems are normally semi-active to avoid operation inefficiencies [20]. Hence, the received data needs to be modified to match the desired fully-active geometry. This can be accomplished by introducing new virtual transmitters, which will follow the same path as the original transmitter but with a certain time delay, as illustrated in Fig. 7. The Rx antenna tracks will be relocated onto the reference receiver track. At this point, it is important to introduce the index  $k$  in the coming expressions to account for the fact that the range-compressed data will be processed in smaller azimuth blocks to reduce the variation over time of the velocity and the 3D baselines. Then, the 3D velocity vector introduced in (5) of an azimuth block  $k$  can be renamed as  $v_k(t)$  and it will differ from block to block. Consequently, the block azimuth direction presented in (6) will be recalculated for each azimuth block ( $u_{azk}$ ). The position of the phase center in the block azimuth direction for the relocated bistatic channels must be the same as in the original semi-active constellation to leave the azimuth sample spacing unchanged. Consequently, the time delays between channels in the semi-active geometry must remain unaltered. The time delay between two bistatic channels in a semi-active configuration can be expressed as:

$$\Delta t_{k,i}(t) = \frac{\Delta d_{k,Rx_i \rightarrow Rx_{ref}}(t)}{\|\bar{v}_k\|} \quad (12)$$

where

$$\Delta d_{k,Rx_i \rightarrow Rx_{ref}}(t) = \Delta b_{k,Rx_i \rightarrow Rx_{ref}}(t) \cdot u_{azk}^T \quad (13)$$

and

$$u_{azk} = \frac{\bar{v}_k}{\|\bar{v}_k\|}. \quad (14)$$

$\Delta d_{k,Rx_i \rightarrow Rx_{ref}}(t)$  is the azimuth projection in a semi-active setup of the relative baseline between the phase center of the reference bistatic track and the phase center of the bistatic track  $i$ , within the block with index  $k$ .  $\Delta b_{k,Rx_i \rightarrow Rx_{ref}}(t)$  is the relative baseline introduced in (3) but defined for a specific azimuth block  $k$ . Finally,  $\bar{v}_k$  is the mean over time of the block 3D velocity vector  $v_k(t)$ .

The concept presented in Fig. 7 can be implemented by using a MoCo algorithm. Then, a phase correction can be applied based on the differences between the original bistatic tracks of the semi-active configuration and the new fully-active bistatic tracks. This MoCo will be referred to as RelMoCo. Summarizing, to transform a semi-active bistatic IRF (as presented in (9)) into a fully-active bistatic IRF (as shown in (10)) motion components need to be included. Then, the bistatic IRF of an azimuth block  $k$  for an arbitrary channel  $i$  within a semi-active DBF SAR configuration can be redefined in the time domain as

$$h_{k,i}(t, r; f_r) = e_{BC_{k,i}}(t, r; f_0) \cdot \text{IFFT}_{f_a \rightarrow t} \left[ G_{k,i}(f_{a_k}, r; f_r) \right] \quad (15)$$

where

$$G_{k,i}(f_{a_k}, r; f_r) = H_{k,ref}(f_{a_k}, r; f_r) \cdot \exp \left[ -j \cdot 2\pi \cdot f_{a_k} \cdot \Delta t_{k,i} \right] \cdot \bar{E}_{D_{k,i}}(f_{a_k}, r; f_r) \quad (16)$$

and

$$\bar{\Delta t}_{k,i} = \text{mean}_t \left( \frac{\Delta d_{k,Rx_i \rightarrow Rx_{ref}}(t)}{\|\bar{v}_k\|} \right). \quad (17)$$

The terms defined in the frequency domain use time-averaged values, which are recalculated for each azimuth block. Since the average velocity  $\bar{v}_k$  is block-dependent, the FDC will also change slightly from block to block. For this reason, the azimuth frequency must be redefined as  $f_{a_k} \in \left[ \frac{-N \cdot PRF}{2} + f_{d_k}, \frac{N \cdot PRF}{2} + f_{d_k} \right]$  to indicate that it varies depending on the azimuth block, where  $f_{d_k}$  is the FDC of the azimuth block with index  $k$ .  $e_{BC_{k,i}}(t, r; f_0)$  is a phase term corresponding to the beam-center range difference due to the change of geometries for the bistatic channel  $i$  and  $\bar{E}_{D_{k,i}}(f_{a_k}, r; f_r)$  is the residual range difference related to the echoes received from different squint angles, averaged over time. The subscripts  $BC$  and  $D$  are used to differentiate between the beam-center and Doppler-dependent phase terms, respectively.  $e_{BC_{k,i}}(t, r; f_0)$  is defined for the transmitted center frequency  $f_r = f_0$  and the beam-center pointing direction corresponding to  $f_{a_k} = f_{d_k}$ . It is important to separate these two terms because they will be corrected in two different domains. The estimation of the range differences will be introduced in sections III.B and III.C, respectively. This way of expressing the bistatic IRF makes the definition more flexible, allowing it to account for time-variant inter-channel baselines and sensor velocity.

Taking (15) and the antenna pattern  $A_k(f_{a_k}, r; f_r)$  into account, the multi-channel SAR signal model interpreted as a fully-active configuration is presented in Fig. 8 as a block diagram. The antenna pattern is in this case assumed to be the same for the three channels and channel 1 is set as the reference bistatic channel. The signal

$$W_{k,ref}(f_{a_k}, r; f_r) = A_k(f_{a_k}, r; f_r) \cdot H_{k,ref}(f_{a_k}, r; f_r) \quad (18)$$

is the reference bistatic SAR signal that is to be recovered after DBF reconstruction. This differs from traditional azimuth reconstructions, where a monostatic SAR signal is set as the reference. The subscript  $k$  indicates that the antenna pattern and reference IRF are re-estimated for each azimuth block separately. Fig. 8 is an example model to illustrate a case where the bistatic channel 1 is identical to the reference but generally every channel could be set as a reference depending on the specific system. Introducing the antenna pattern in (15), the SAR signal for an arbitrary DBF bistatic channel  $i$  is expressed in this proposal as

$$s_{k,i}(t, r; f_r) = e_{BC_{k,i}}(t, r; f_0) \cdot \text{IFFT}_{f_a \rightarrow t} \left[ W_{k,i}(f_{a_k}, r; f_r) \right] \quad (19)$$

where

$$W_{k,i}(f_{a_k}, r; f_r) = A_k(f_{a_k}, r; f_r) \cdot G_{k,i}(f_{a_k}, r; f_r). \quad (20)$$

### B. Beam-Center Motion Compensation

First, the beam-center component  $e_{BC_{k,i}}(t, r; f_0)$  must be removed from the data. For this, a beam-center MoCo algorithm can be used to do a phase correction in the time domain

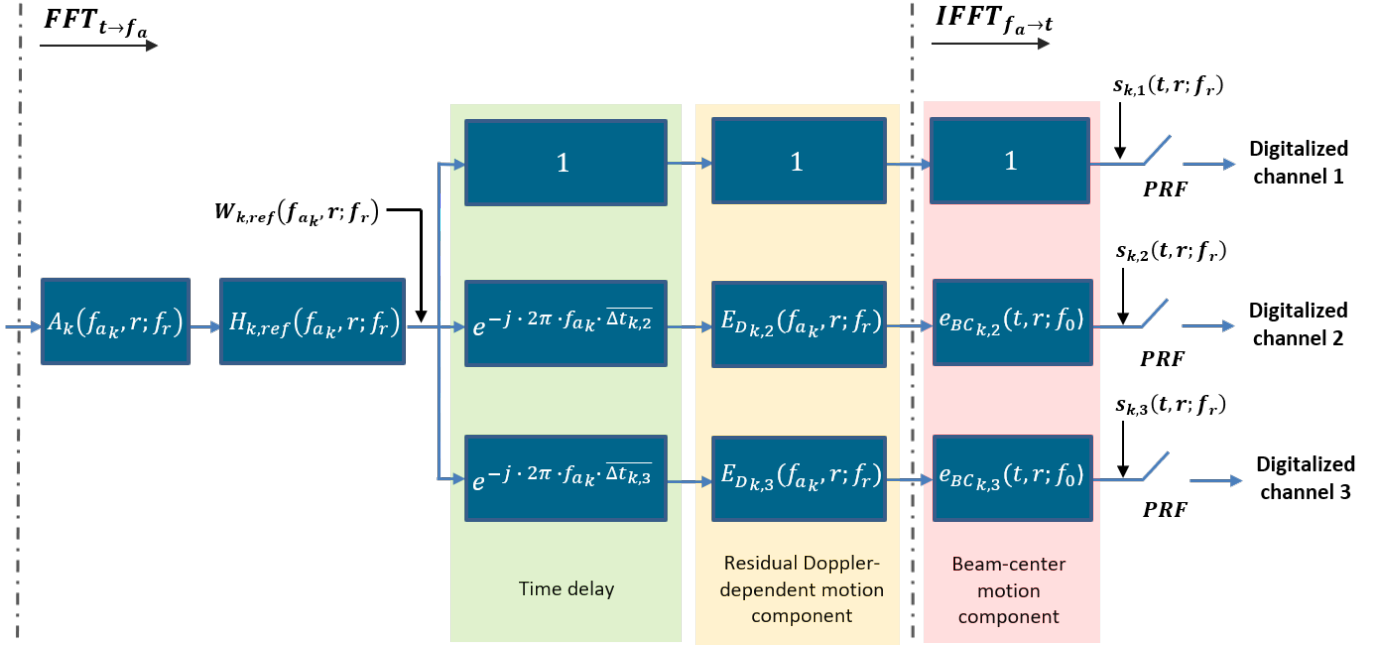


Fig. 8. Example of the signal model for an arbitrary azimuth block  $k$  in a multi-static SAR system with three channels where the channels are defined as delayed versions of one of the bistatic channels with additional motion components. The time delay and the Doppler-dependent residual motion component are defined in the range-Doppler domain and the beam-center motion component is defined in the time domain.

of each dataset. This technique uses a similar approach as the one-step MoCo presented in [39].

Before implementing a MoCo technique, it is necessary to determine the line-of-sight (LOS) differences between the real and relocated tracks for the points in space corresponding to each sample of the slant range grid. The LOS differences are estimated separately for Rx and Tx. Knowing the inter-channel azimuth baselines presented in (13) for the desired fully-active constellation, the relocated Rx and Tx tracks for an arbitrary azimuth block  $k$  can be easily obtained as

$$q_{k,Rx_i}(t) = q_{k,Rx_{ref}} \left( t - \frac{\Delta d_{k,Rx_i}^{az} Rx_{ref}(t)}{\|\bar{v}_k\|} \right) \quad (21)$$

and

$$q_{k,Tx_i}(t) = q_{k,Tx} \left( t - \frac{\Delta d_{k,Rx_i}^{az} Rx_{ref}(t)}{\|\bar{v}_k\|} \right) \quad (22)$$

respectively.

Using a DEM the LOS distance ( $R_{k,\psi}(t, f_{a_k}, r)$ ) between each point in the scene and the respective point in the track of the desired aperture  $\psi$  can be obtained as

$$R_{k,\psi}(t; f_{a_k}, r) = \|q_{k,\psi}(t) - DEM_k(t; f_{a_k}, r)\| \quad (23)$$

where  $DEM_k(t, r; f_{a_k})$  denotes the position of each point of the grid used to represent the terrain topography estimated for the azimuth block  $k$ . The DEM is not only defined for each azimuth sample and slant range but also for different squint angles (dependency on  $f_{a_k}$ ). This additional degree of freedom allows to calculate the estimated residual phase errors of the beam-center RelMoCo, which is just defined for the Doppler centroid  $f_{d_k}$ . Accordingly, when backgeocoding the DEM for

the beam-center RelMoCo, the processed squint angle ( $\hat{\theta}$ ) must be known to obtain the value of  $f_{d_k}$  as

$$f_{d_k} = \frac{2 \cdot \|\bar{v}_k\| \cdot \sin \hat{\theta}}{\lambda} \quad (24)$$

where  $\lambda$  indicates the wavelength of the center frequency. The value of  $\hat{\theta}$  does not depend on the azimuth block and is constant over time.

Then, the LOS differences between real and relocated Rx tracks to a certain point at a range  $r$  can be expressed as

$$\Delta R_{k,Rx_i}(t; f_{d_k}, r) = R_{k,Rx_i}(t; f_{d_k}, r) - R_{k,Rx_i}(t; f_{d_k}, r) \quad (25)$$

where  $R_{k,Rx_i}(t; f_{d_k}, r)$  is the LOS distance between the position of the original Rx antenna track for channel  $i$  and the specific point on the ground.  $R_{k,Rx_i}(t; f_{d_k}, r)$  is the same but for the relocated Rx antenna track.

The LOS differences for Tx aim to account for the generation of virtual transmitters to define the system geometry as a fully-active constellation. As in (25), the LOS differences in Tx can be calculated as

$$\Delta R_{k,Tx_i}(t; f_{d_k}, r) = R_{k,Tx}(t; f_{d_k}, r) - R_{k,Tx_i}(t; f_{d_k}, r) \quad (26)$$

where  $R_{k,Tx}(t; f_{d_k}, r)$  is the LOS distance between the position of the real Tx antenna track and the point on the ground.  $R_{k,Tx_i}(t; f_{d_k}, r)$  expresses this distance but for the new virtual Tx antenna track.

The corresponding beam-center phase correction for each point in the dataset can be defined as

$$e_{BC_{k,i}}(t, r; f_0) = \exp \left[ -j \cdot \frac{2\pi \cdot f_0}{c_0} \cdot \Delta R_{BC_{k,i}}(t, r) \right] \quad (27)$$

where

$$\Delta R_{BC_{k,i}}(t, r) = \Delta R_{k,Rx_i}(t; f_{d_k}, r) + \Delta R_{k,Tx_i}(t; f_{d_k}, r). \quad (28)$$

Supposing a subsampled range-compressed 2D dataset  $s_{k,i}(t, r; f_r)$ , the beam-center corrected data can be defined as:

$$\hat{s}_{k,i}(t, r; f_r) = \frac{\tilde{s}_{k,i}(t, r; f_r)}{e_{BC_{k,i}}(t, r, f_0)} \quad (29)$$

where

$$\tilde{s}_{k,i}(t, r, f_r) = s_{k,i}(t, r + \frac{\Delta R_{BC_{k,i}}(t, r)}{2}; f_r). \quad (30)$$

Since the phase correction is range-dependent, an interpolation of the channel data needs to be performed before this correction happens, as expressed in (30). This reduces the residual phase error arising from the non-polychromatic definition of  $e_{BC_{k,i}}(t, r; f_0)$ , which is just defined for the transmitted center frequency.

### C. New Azimuth Reconstruction

After the beam-center RelMoCo, the data has been corrected for the squint angle corresponding to the FDC ( $f_{d_k}$ ). This leaves an unwanted residual error in the Doppler domain related to the received echoes coming from the remaining squint angles according to the Doppler bandwidth. State-of-the-art MoCo algorithms can address these errors but they assume a non-aliased azimuth spectrum, which is not the case for systems based on a multiple azimuth phase center sampling (MAPS). To overcome this limitation, the solution proposed in this section introduces the residual Doppler motion component  $\bar{E}_{D_{k,i}}(f_{a_k}, r; f_r)$  in the definition of the bistatic IRF, as shown in (16). The expected residual phase error includes the LOS range differences for every Doppler frequency in the interval  $f_{a_k} \in [f_{d_k} - \frac{N \cdot PRF}{2}, f_{d_k} + \frac{N \cdot PRF}{2}]$ . By necessity, the residual phase errors will be calculated using the LOS ranges introduced in (23) averaged over time  $\bar{R}_{k,\psi}(f_{a_k}, r)$  for each frequency  $f_{a_k}$ , since in the Doppler domain there is no azimuth spatial resolution. Then, the Doppler-dependent LOS range differences can be defined as

$$\Delta \bar{R}_{k,Rx_i}(f_{a_k}, r) = \bar{R}_{k,Rx_i}(f_{a_k}, r) - \bar{R}_{k,Rx_i}^{\sim}(f_{a_k}, r) \quad (31)$$

for Rx and

$$\Delta \bar{R}_{k,Tx_i}(f_{a_k}, r) = \bar{R}_{k,Tx_i}(f_{a_k}, r) - \bar{R}_{k,Tx_i}^{\sim}(f_{a_k}, r) \quad (32)$$

for Tx, where

$$\bar{R}_{k,\psi}(f_{a_k}, r) = \text{mean}_t(R_{k,\psi}(t; f_{a_k}, r)). \quad (33)$$

To calculate the residual error, the LOS range differences in Rx and Tx used in the beam-center RelMoCo must be subtracted from (31) and (32), respectively. Gathering all this information, the residual phase error can be expressed as

$$\bar{E}_{D_{k,i}}(f_{a_k}, r; f_r) = \exp \left[ -j \cdot \frac{2\pi \cdot f_r}{c_0} \cdot \Delta \bar{R}_{k,i}(f_{a_k}, r) \right] \quad (34)$$

where

$$\Delta \bar{R}_{k,i}(f_{a_k}, r) = \Delta \bar{R}_{D_{k,i}}(f_{a_k}, r) - \text{mean}_t(\Delta R_{BC_{k,i}}(t, r)) \quad (35)$$

and

$$\Delta \bar{R}_{D_{k,i}}(f_{a_k}, r) = \Delta \bar{R}_{k,Rx_i}(f_{a_k}, r) + \Delta \bar{R}_{k,Tx_i}(f_{a_k}, r). \quad (36)$$

In (35) the residual LOS range differences are calculated by subtracting the average over  $t$  of the LOS range differences presented in (28) to the Doppler-dependent range differences obtained in (31) and (32). This is an approximation as it assumes that the variation over the slow time of the RelMoCo correction is negligible, which may not be true for large blocks. Therefore, it is recommended to keep the size of the azimuth blocks as small as possible but with enough samples to achieve a certain frequency resolution in the Doppler domain. In practice, the Doppler domain resolution must be high enough to accommodate the desired application, as will be discussed more in detail in Section IV-A.

As shown in [5], the azimuth reconstruction does not just suppress the azimuth ambiguities but also removes the channel-specific components that are defined in the bistatic IRF. The only components in the bistatic IRF that are not removed after the reconstruction are the ones that are common among the channels. In the case of the IRF defined in (16), the only common factor among the channels is  $H_{k,ref}(f_{a_k}, r; f_r)$  which is the original bistatic IRF of the bistatic channel that was set as reference. After applying a beam-center correction to the IRF of equation (19), the channel-specific component of the bistatic IRF, which will be compensated after reconstruction, can be expressed as:

$$\Gamma_{k,i}(f_{a_k}, r; f_r) = \exp \left[ -j \cdot 2\pi \cdot f_{a_k} \cdot \bar{\Delta} t_{k,i} \right] \cdot \bar{E}_{D_{k,i}}(f_{a_k}, r; f_r). \quad (37)$$

Another important consideration is the polychromatic character of the motion residual phase errors since their values change with  $f_r$ . In other words, since the transmitted chirp has a certain bandwidth, a SAR signal is composed of different range frequency components, which will propagate slightly differently from each other. The solution chosen in this investigation is to implement a two-step reconstruction, as presented in [7], [8]. This enhances the reconstruction algorithm by first processing the undersampled channel  $i$  with a filter in the wavenumber domain  $P_{k,i}(f_{a_k}, r_{ref}; f_r)$  and afterward with another reconstruction filter in the range-Doppler domain  $\Delta P_{k,i}(f_{a_k}, r; f_0)$ . The multi-channel SAR matrix ( $\Gamma_k(f_{a_k}, r; f_r)$ ) can be defined as a row vector with  $N$  elements:

$$\Gamma_k(f_{a_k}, r; f_r) = [\gamma_{k,1}(f_{a_k}, r; f_r) \quad \dots \quad \gamma_{k,N}(f_{a_k}, r; f_r)] \quad (38)$$

where  $\gamma_{k,i}(f_{a_k}, r; f_r)$  is a column vector:

$$\gamma_{k,i}(f_{a_k}, r; f_r) = \begin{bmatrix} \Gamma_{k,i}(f_{a_k}, r; f_r) \\ \Gamma_{k,i}(f_{a_k} + PRF, r; f_r) \\ \vdots \\ \Gamma_{k,i}(f_{a_k} + (N-1) \cdot PRF, r; f_r) \end{bmatrix}. \quad (39)$$

Consequently, the matrix  $\Gamma_k(f_{a_k}, r; f_r)$  has a size of  $N \times N$ , where  $N$  is the number of receiving channels. The reconstruc-

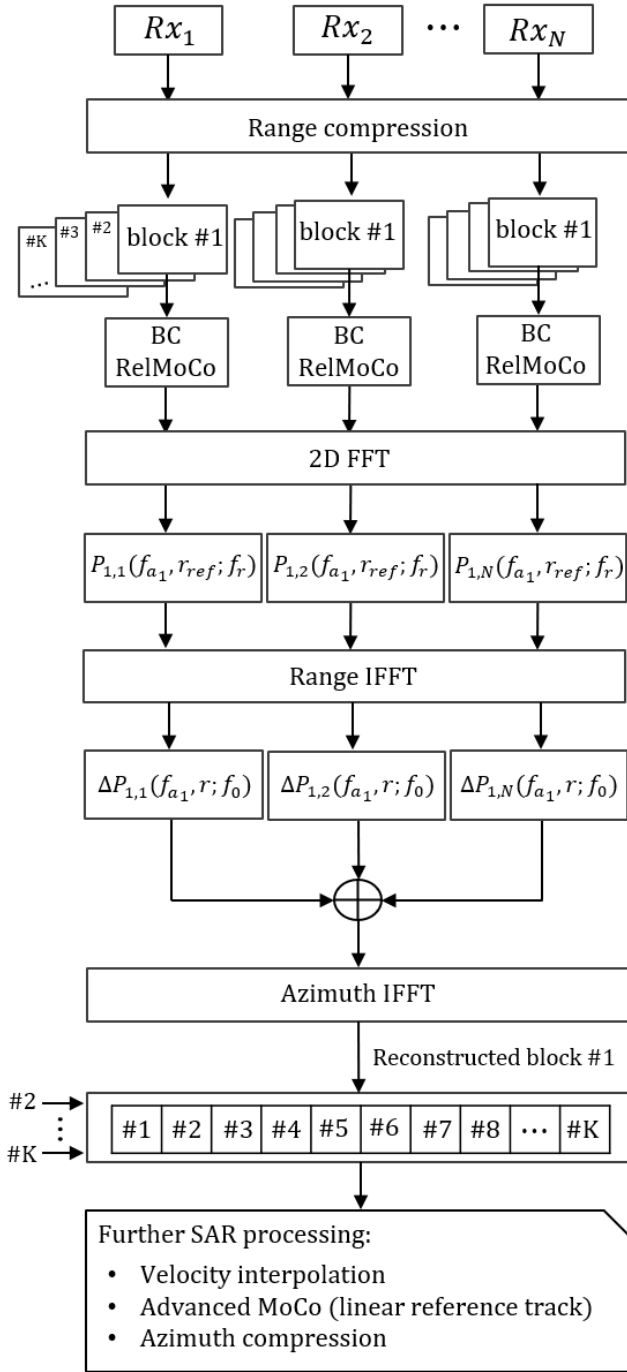


Fig. 9. The block diagram presents a simplified version of the proposed algorithm to process undersampled channels in a DBF SAR airborne system. The constant index 1 in the reconstruction filters denotes that the filters were calculated to process the azimuth block with index  $k = 1$ .

tion filters can be derived from this matrix by calculating its inverse, which will be a new matrix  $N \times N$ , as presented in [5].

$$P_k(f_{a_k}, r; f_r) = \Gamma_k(f_{a_k}, r; f_r)^{-1} \quad (40)$$

Consequently, there will be a matrix  $P$  for each combination of  $f_{a_k}$ ,  $f_r$ , and  $r$ . In Fig. 9 a simplified block diagram of the processing steps before conventional processing is depicted. After compressing the channel data in range, the data of each channel is separated into smaller azimuth blocks or sub-

apertures to reduce the variation of the inter-channel baselines and the velocity within a single block. It is recommended to set a certain overlap between the different azimuth blocks to avoid discontinuities at the edges of each block. The average velocity is recalculated for each block to achieve a more accurate reconstruction. Using sub-apertures also allows the algorithm to perform a more accurate estimation of the Doppler-dependent motion component, as mentioned at the beginning of this sub-section. Furthermore, the decomposition of the range-compressed image in blocks will allow the parallelization of the process to reduce the overall computational time.

After the beam-center RelMoCo is applied separately to each block, the motion-compensated data are transformed into the wavenumber domain. Then, the data are processed by the first bank of reconstruction filters  $P_i(f_{a_k}, r_{ref}; f_r)$ . To do so, the filters are extracted from the respective matrix  $P(f_{a_k}, r_{ref}; f_r)$ , where  $i$  identifies the processed channel and  $r_{ref}$  is the reference slant range, commonly placed in the middle of the scene. Refer also to [5] for details concerning the definition of the reconstruction filters based on the multi-channel SAR matrix. After converting back to the range-Doppler domain, the second bank of reconstruction filters is applied. In this case, the filters must account for the changes already performed in the first bank of reconstruction filters. The second bank of filters is defined as

$$\Delta P_{k,i}(f_{a_k}, r; f_0) = \frac{P_{k,i}(f_{a_k}, r; f_0)}{P_{k,i}(f_{a_k}, r_{ref}; f_0)}. \quad (41)$$

As explained in [7], the two-step azimuth reconstruction enhances the performance of classical reconstruction filters such as the one presented in [5] since it accounts not only for the dependence on the slant range but also for the dependence on the range frequency.

After the second bank of filters, the reconstruction result is obtained by transforming the coherent sum of all filtered channel spectra back into the time domain. Since the image was divided initially into  $K$  azimuth blocks, there will be a total of  $K$  reconstructions, rearranged to form a new range-compressed 2D SAR signal that will be passed to the SAR processor to form a properly focused SAR image. The overlap between blocks must also be considered when rearranging the output reconstructed azimuth blocks. In this case, the redundant azimuth samples at the edges of the block are simply discarded. As indicated in (12), the average velocity can change from block to block, meaning that the bistatic IRF might be different in each azimuth block. This fact can introduce phase discontinuities between contiguous reconstructed blocks. Nevertheless, these discontinuities can be shown to be negligible (i.e., less than 0.5 degrees) in this investigation, as the block size is chosen to be small enough so that the variation in average velocity between the blocks is minor.

#### IV. EXPERIMENTS AND RESULTS

In this section, several tests are presented to demonstrate the advantages of the proposed reconstruction algorithm for DBF SAR airborne systems. First, a simulated point target is generated based on the information from the real multi-channel SAR system configuration used in the flight presented

TABLE I  
PARAMETERS POINT TARGET SIMULATION

Parameter	Value
Carrier frequency	9.50 GHz
Chirp bandwidth	400.00 MHz
Range sampling frequency	500.00 MHz
Processed squint angle	-2.83°
PRF	150.24 Hz
Azimuth bandwidth	400.00 Hz
Target altitude	768.36 m
Average sensor altitude	3050.00 m
Mean velocity	90.11 m/s
Number of receivers	3

TABLE II  
COMPARISON OF AASR FOR THE CONFIGURATIONS SHOWN IN FIG. 11

	No RelMoCo	BC RelMoCo	Full RelMoCo
AASR: $Amb_{-2}$	-11.20 dB	-51.25 dB	-53.18 dB
AASR: $Amb_{-1}$	5.61 dB	-48.03 dB	-60.84 dB
AASR: $Amb_{+1}$	-5.36 dB	-44.28 dB	-61.15 dB
AASR: $Amb_{+2}$	-3.11 dB	-48.29 dB	-60.81 dB

TABLE III  
SIMULATION: OTHER IMPORTANT PERFORMANCE PARAMETERS

	No RelMoCo	BC RelMoCo	Full RelMoCo	Reference
RCS	33.75 dB	42.57 dB	42.57 dB	42.60 dB
ISLR	-6.01 dB	-5.80 dB	-5.80 dB	-5.83 dB
$\delta_{az}$	30.37 cm	30.10 cm	30.11 cm	30.11 cm

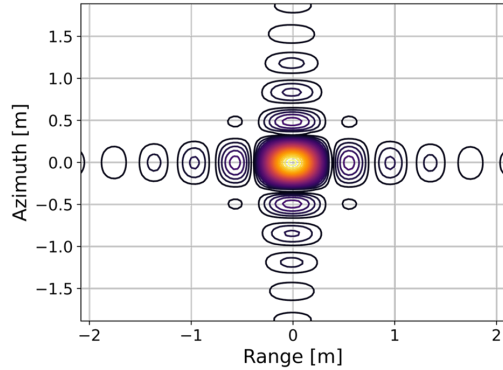


Fig. 10. Imaging result of the simulated point target for the reconstruction using the proposed full RelMoCo algorithm. The outermost contour level corresponds to a signal level of -28.10 dB relative to the peak.

in Section II. Here the impact of uncorrected residual phase errors, inaccuracies in the DEM, and velocity variations on the performance of the reconstruction is discussed by analyzing the AASR and the computational effort. Then, the raw data obtained in the real experiment is reconstructed to verify the results obtained in the simulations.

#### A. Point Target Simulation

Using the information of the campaign conducted with the DLR DBFSAR airborne system presented in Section II a point target simulation was generated based on the deployed reflectors' coordinates during the campaign. The real across-track motion, attitude angles, and velocity variations of the flight pass were kept as they were originally. Nevertheless, the simulated data differs from the real acquisition in several

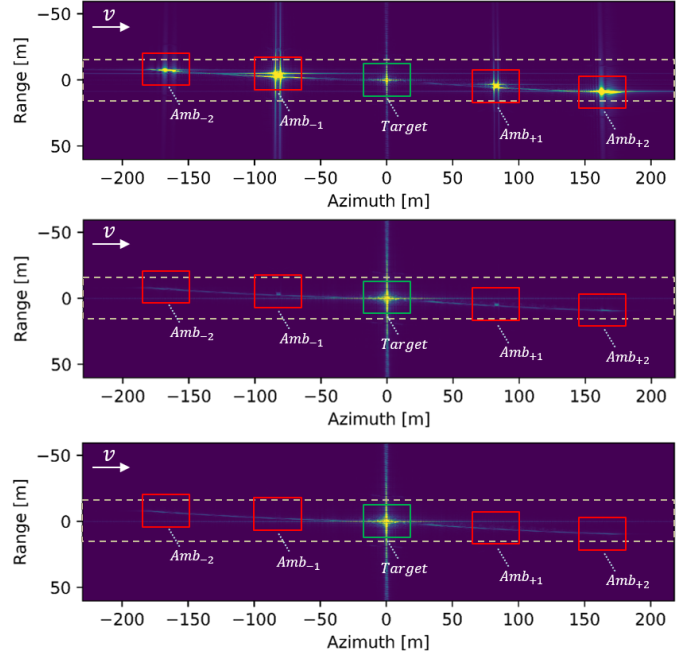


Fig. 11. Simulated focused reconstructed SAR images using different configurations for the algorithm. Reconstruction without any previous RelMoCo (top). Reconstruction applying the beam-center RelMoCo (middle). Reconstruction using both beam-center and Doppler-dependent RelMoCo (bottom). The red/green rectangles indicate the integration footprint used for the ambiguous/signal power to compute the AASR. The dotted square indicates the area in which the power of the range bins was integrated to obtain Fig. 12. The flight direction of the linear reference track after azimuth focusing is indicated on the upper left side of each image.

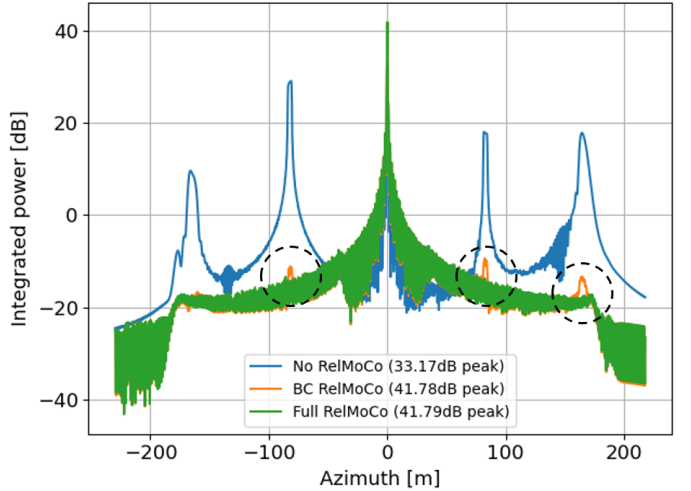


Fig. 12. Representation of the azimuth ambiguities after integrating the power of the range bins in the dotted area depicted in Fig. 11. The dotted circles highlight the residual azimuth ambiguities connected to uncompensated Doppler-related motion inconsistencies. The peak power of each reconstructed point target is shown in the legend.

respects: First, the PRF was reduced to force the dataset to be undersampled since the real acquisition was oversampled. Additionally, the simulation imposed a constant (isotropic) antenna pattern for all channels to remove antenna-related effects from the study. Finally, factors such as thermal noise, the troposphere, or coastline scenarios with high land clutter

were considered to be beyond the scope of this investigation and assumed to be of secondary importance for the DBF SAR system configuration under study. The parameters used to run the simulation are listed in Table I.

In Fig. 11 the results of this experiment are depicted. The subsampled channels generated using the configuration in Table I were processed by three different reconstruction setups and then focused using the standard airborne SAR processor of DLR. The processor was set to obtain a nominal azimuth resolution ( $\delta_{az}$ ) of 0.3 m. The algorithm separated the range-compressed image in azimuth blocks of 64 samples with an overlap of 8 samples between adjacent blocks. A flat DEM was utilized to calculate the LOS range differences, where the height was set equal to the height of the target under study. The first reconstruction (top plot in Fig. 11) was equivalent to a classic DBF azimuth reconstruction, as used in [5], where no RelMoCo was applied before reconstruction. Then a second reconstruction algorithm (middle plot in Fig. 11) was used, where the beam-center RelMoCo (see Section III-B) was included but the Doppler-dependent RelMoCo (see Section III-C) factor was omitted in the reconstruction filters. Finally, the last reconstruction (bottom plot in Fig. 11) included all the RelMoCo components presented in Section III. This last configuration will be referred to as full RelMoCo in this section. In Fig. 10 a zoom of the reconstructed focused point target after using the full RelMoCo is depicted. The azimuth resolution achieved in this case was very close to the nominal value of 0.3 m, as shown in Table III.

The AASR for each setup and each ambiguity is shown in Table II. To calculate the AASR accurately the output geometry and the output PRF were given to the simulator to generate an ideal point target to obtain an ambiguity-free range-compressed signal which then was also focused. The absolute value of the ambiguity-free image was then subtracted in each of the focused reconstructed images to separate ambiguity and target integrated power. This approach improves the accuracy of the AASR determination considerably, as it eliminates the bias that would otherwise be introduced by the power of the target response sidelobes. The areas delimited by the red squares in Fig. 11 show approximately the integration areas to obtain the ambiguous power that was then used to calculate the AASR. A similar area (green square) around the target was used to integrate the power of the target itself.

Fig. 12 depicts a 1D plot after integrating the power of the range bins in the areas delimited by the dotted rectangles in Fig. 11. The results show that not applying any motion compensation before reconstruction leads to a poor performance in terms of ambiguity suppression with one of the ambiguities even exceeding the actual target power (AASR > 0 dB). The asymmetry in the ambiguous power over azimuth is related to uncorrected phase errors and the influence of the FDC. Including the beam-center RelMoCo in the process improves the performance considerably but residual ambiguities are still visible in the image due to uncorrected phase errors in the Doppler domain. Finally, the configuration using a full RelMoCo shows the best results, where the ambiguities are no longer visible. Table II shows that the best AASR is achieved when the reconstruction implements the full RelMoCo. The

AASR for the second-order azimuth ambiguity on the left (Amb<sub>-2</sub>) seems to be higher than the rest of the values in the column of Table II corresponding to the full RelMoCo. However, looking at the shape of the green line in Fig. 12, there is no visible ambiguous power in the area corresponding to this second-order ambiguity. Therefore, it was concluded that the values of the AASR for this ambiguity do not come from ambiguous power but from a mismatch between the sidelobe of the reconstructed target and the simulated ambiguity-free target at the edges of the range history.

Comparing the peak powers (see legend in Fig. 12) one can see that after azimuth compression the green-colored point target achieves a peak signal power 8.62 dB higher than the blue-colored point target. Hence, not using any RelMoCo technique can also deteriorate considerably the radiometric accuracy and signal-to-noise (SNR) ratio. The values of other important performance parameters are listed in Table III. Additionally, Table III includes the performance parameters obtained with a reference image. This reference is generated using the same geometry as the simulation but with the original operational PRF of 3004.80 Hz. This signal did not need any reconstruction and was directly processed to obtain a nominal resolution of 0.3 m, as with the outputs of the reconstructions. The radar cross section (RCS) of the target indicates that not using any RelMoCo technique during the reconstruction can lead to a considerable loss of energy. On the other hand, the integrated sidelobe ratio (ISLR) seems not to be significantly affected by the fact of using or not a RelMoCo technique during the reconstruction. Finally, the azimuth resolution obtained after the reconstruction using the proposed RelMoCo technique was almost identical to the one achieved by the reference.

To prove the effectiveness of the algorithm over the entire swath width, two additional point targets were added to the simulation. Each of them was placed at a different range and azimuth position. The new multi-channel subsampled dataset was passed to the reconstruction algorithm, where first a reconstruction was performed without including the RelMoCo. Afterward, the same dataset was reconstructed using both beam-center and Doppler-dependent RelMoCo. The reconstructed simulated point targets after azimuth compression are depicted in Fig. 13. Table IV shows the worst AASR obtained for each of the three targets in both scenarios. The results of the experiment confirm that the reconstruction using the full RelMoCo has excellent results along the whole swath.

The next experiment aims to analyze the sensitivity of the proposed RelMoCo to inaccuracies in the DEM. In this experiment, the simulated point target was reconstructed using a full RelMoCo where the value used to define the terrain height of the flat DEM was modified by adding different offsets. The target was located at a height of 768.36 m above the WGS84 ellipsoid. The results shown in Fig. 14 suggest that the algorithm is very sensitive to mismatches between the actual height of the target and the terrain height set in the DEM used in the RelMoCo, degrading the AASR by almost 35 dB in the worst-case scenario analyzed in this test. Evaluating the peak power of the signal relative to the minimum clutter level in the real scene (see Fig. 19), a conservative threshold of -

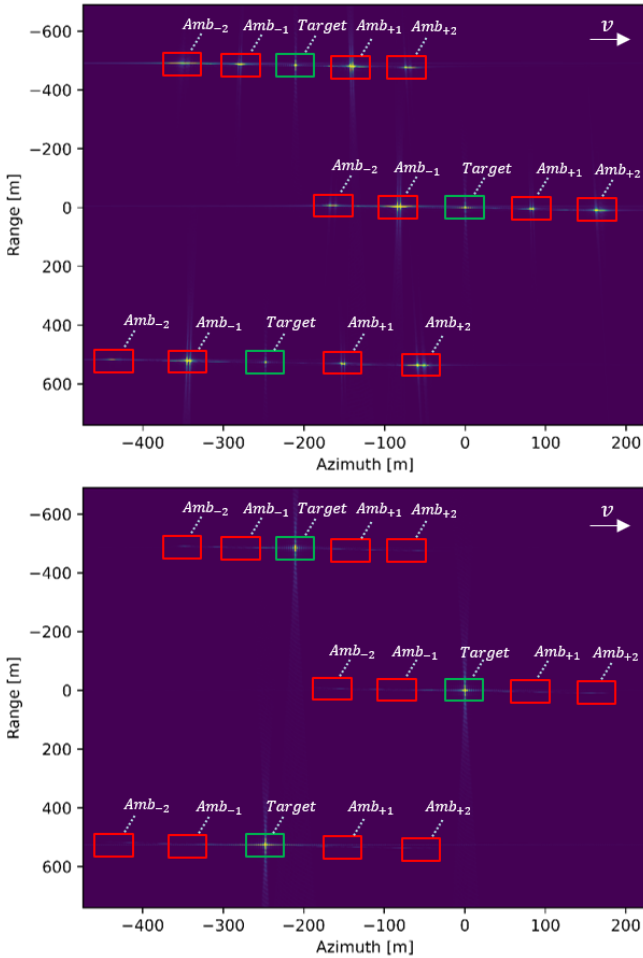


Fig. 13. Simulated focused reconstructed SAR point targets placed at different slant ranges. The range axis corresponds to an off-nadir angle range of 20.82 to 57.36 degrees. The relation between off-nadir angle and range is not linear. Reconstruction without any previous RelMoCo (top). Reconstruction using both beam-center and Doppler-dependent RelMoCo (bottom). The red/green rectangles indicate the integration footprint used for the ambiguous/signal power to compute the AASR. The flight direction of the linear reference track after azimuth focusing is indicated on the upper right side of each image.

TABLE IV

SIMULATION: COMPARISON OF AASR ALONG THE SWATH IN FIG. 13

Range	Near-Range	Mid-Range	Far-Range
Max. AASR (No RelMoCo)	5.45 dB	5.63 dB	9.81 dB
Max. AASR (Full RelMoCo)	-59.67 dB	-61.79 dB	-60.61 dB

50 dB was set for the AASR to consider the reconstruction acceptable. According to the results of Fig. 14, this translates into a DEM accuracy requirement of  $\pm 3$  m. Therefore, the RelMoCo step in the reconstruction must, in practice, use an accurate real DEM if a SAR image with strong changes in the topography is to be successfully reconstructed. The asymmetry observed in Fig. 14 along the DEM height axis results from the uncorrected motion irregularities, which are not symmetric over azimuth (see Fig. 4), and from the ambiguity asymmetry inherent in SAR systems with a strong FDC (see Fig. 12).

Subsequently, the impact of velocity variations within an azimuth block was assessed. Fig. 15 (top left) depicts the velocity of the sensor over the illumination time of the target.

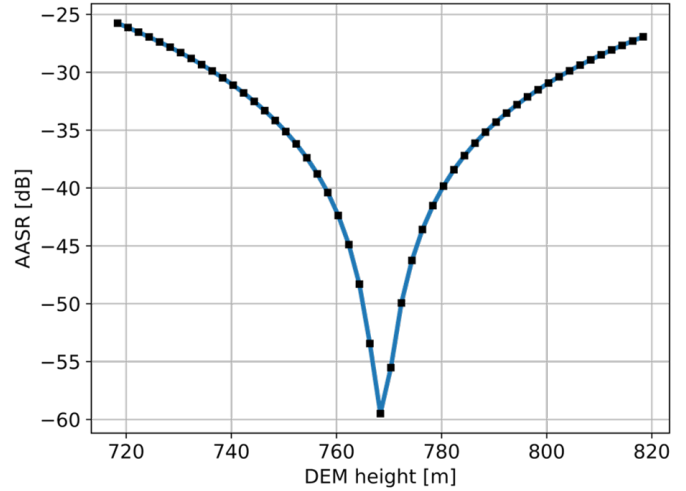


Fig. 14. Performance analysis of the reconstruction when the height of the flat DEM is modified in steps of 2 m for the calculation of the RelMoCo correction factors. The target was located at a terrain height of 768.36 m. The AASR corresponds to the strongest azimuth ambiguity in each reconstruction.

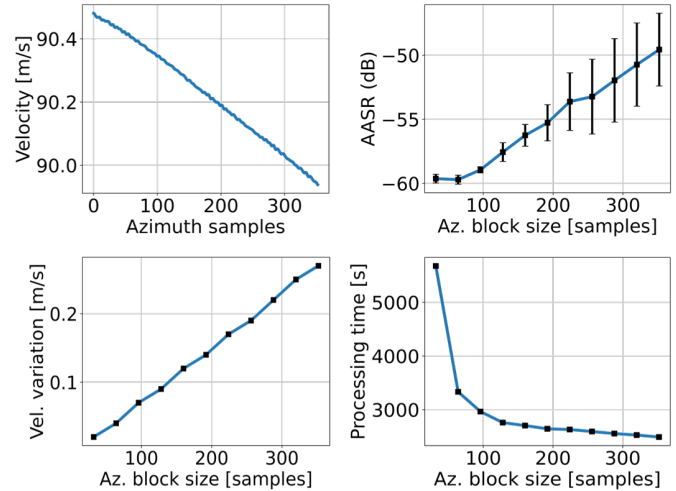


Fig. 15. Results of the simulations to test the impact of velocity variations on the performance of the reconstruction algorithm: Real velocity of the sensor along the synthetic aperture while the target was recorded. This is an extraction from Fig. 5 (top left). Estimation of the average velocity variation within a single azimuth block for different block sizes based on the velocity variation of the sensor along the synthetic aperture (bottom left). Average AASR over the chosen azimuth block size. The error bars show the standard deviation of the collected results (top right). Computational time for a reconstruction using full RelMoCo depending on the azimuth block size (bottom right).

The azimuth extent of the simulation corresponds to a small fraction of the total scene size (compare Fig. 15 and Fig. 5). Considering that for this specific target the velocity varies almost linearly with the time, an expectation of the average velocity variability within a block can be calculated. Fig. 15 (bottom left) shows the expected velocity mismatch within a single block for different block sizes.

The top right plot of Fig. 15 illustrates the impact of azimuth block size on the reconstruction quality as measured in terms of the AASR. For this experiment different reconstructions were performed using different block sizes, then all the results were focused and the AASR was calculated. From

TABLE V  
AASR AFTER SETTING DIFFERENT VELOCITIES FOR THE DBF FILTERS

Velocity	88.2 m/s	89.2 m/s	90.2 m/s	91.2 m/s	92.2 m/s
AASR: Amb <sub>-2</sub>	-44.51 dB	-49.15 dB	-53.20 dB	-50.89 dB	-46.41 dB
AASR: Amb <sub>-1</sub>	-31.15 dB	-36.86 dB	-55.96 dB	-38.78 dB	-32.11 dB
AASR: Amb <sub>+1</sub>	-25.80 dB	-32.89 dB	-48.34 dB	-30.41 dB	-24.89 dB
AASR: Amb <sub>+2</sub>	-35.07 dB	-43.42 dB	-51.94 dB	-37.44 dB	-32.11 dB

the outcome, the worst AASR was picked. This was repeated five times. Each time the size of the first block was modified to change the center of the blocks to obtain a set of results that better show the trend of the performance related to the block size. The AASR of the second-order ambiguity on the left (Amb<sub>-2</sub>) was ignored in this investigation since it is not considered to be entirely related to ambiguous power, as mentioned before. The blue line is the average AASR for each block size. The error bars show the standard deviation of the results. As it was expected, the best and most consistent results are obtained for block sizes, where the velocity variation is smaller. The results reveal that a block size of 32 samples does not further improve the ambiguity suppression compared to the reconstruction performed using blocks of 64 samples.

The computational effort is also important to be considered to optimize the available resources. For this reason, the computational time of a reconstruction using full RelMoCo without using parallel processing is depicted in Fig. 15 (bottom right). The results suggest that using a block size of 64 to 128 samples represents a reasonable trade-off between quality and computation time for this particular airborne SAR geometry. However, if parallel block processing is possible, the reconstruction computational time will be reduced considerably.

Nevertheless, block processing does not just affect the velocity variation but also other factors such as the resolution of the Doppler spectrum and the accuracy of the Doppler-dependent RelMoCo factor. Consequently, the next test aims to isolate the influence of velocity mismatches in an azimuth reconstruction. For this experiment, five different reconstructions using the proposed full RelMoCo were performed. In this case, an azimuth block size of 64 samples was used for all the reconstructions. Instead of calculating the average velocity for each block, the value was kept constant for all the blocks. Then, for each test, the velocity value used to define the reconstruction filters was modified by adding offsets to the average velocity of the sensor. The average value for the center velocity was set to 90.2 m/s, which is the optimum value according to Fig. 15 (top left). The numerical results of this study are listed in Table V. The corresponding results of Fig. 16 show that even an error of  $\pm 1$  m/s in the definition of the reconstruction filters affects the performance of the reconstruction. The offsets of  $\pm 1$  m/s and  $\pm 2$  m/s were selected based on the variations observed in Fig. 5. Furthermore, it can be observed that even a perfect estimation of the sensor speed does not achieve a complete ambiguity suppression for the first-order azimuth ambiguity on the right (Amb<sub>+1</sub>). The reason is that the velocity was set constant for all blocks, which would be similar to processing the image without any block processing. In other words, the velocity mismatch in an azimuth block got bigger the farther the block

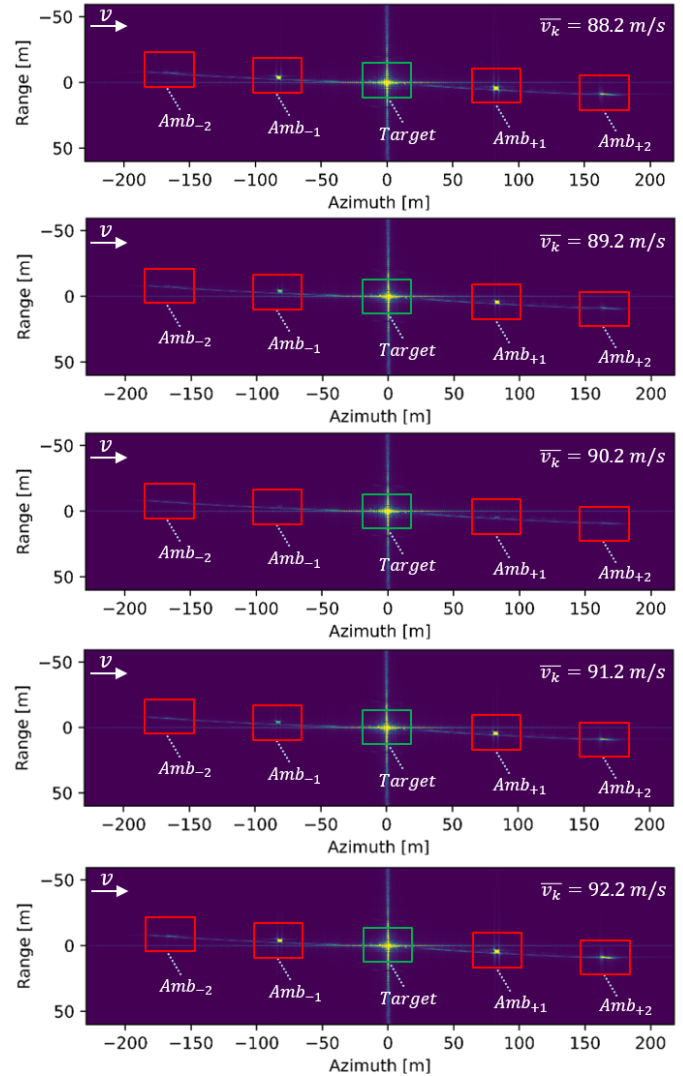


Fig. 16. Focused reconstructed point targets using different constant values for the sensor velocity in the bistatic IRF used to build the DBF filters. The values used for the average block velocity are indicated in the upper right side of each image. The flight direction of the linear reference track after azimuth focusing is indicated on the upper left side of each image. The red/green rectangles indicate the integration footprint used for the ambiguous/signal power to compute the AASR.

center was from the center of the target. This does not just show the necessity to recalculate the average velocity in each block but it also means that the bigger the block size the higher the chances of using a critical velocity mismatch.

### B. Experiment with Real DBFSAR Data

The experiment shown in this section aims to validate the results obtained in the simulation. Originally the channels for this experiment were oversampled, and the bandwidth in azimuth was larger. For this reason, the range-compressed data needed an extra pre-processing step to obtain a comparable scenario to the one presented in the simulation. Originally the system PRF was 3004.80 Hz, so to obtain a PRF equal to the simulation a subsampling factor of 20 needed to be applied. With this, the system PRF was reduced to 150.24 Hz by discarding all but every 20th range line in the original raw

TABLE VI  
PARAMETERS DBFSAR EXPERIMENT

Parameter	Value
Carrier frequency	9.50 GHz
Chirp bandwidth	400.00 MHz
Range sampling frequency	500.00 MHz
Processed squint angle	-2.83°
Original PRF	3004.80 Hz
Subsampling factor in azimuth	20
Azimuth bandwidth (after LPF)	400.00 Hz
Average terrain height	835.25 m
Mean velocity	90.11 m/s
Number of receivers	3

TABLE VII  
COMPARISON OF AASR FOR THE CONFIGURATIONS SHOWN IN FIG. 18

Configuration	No RelMoCo	BC RelMoCo	Full RelMoCo
AASR: Amb <sub>-2</sub>	-11.78 dB	-36.38 dB	-36.52 dB
AASR: Amb <sub>-1</sub>	5.08 dB	-37.55 dB	-37.65 dB
AASR: Amb <sub>+1</sub>	-5.26 dB	-36.16 dB	-37.69 dB
AASR: Amb <sub>+2</sub>	-3.02 dB	-34.01 dB	-34.48 dB

TABLE VIII  
REAL EXPERIMENT: OTHER IMPORTANT PERFORMANCE PARAMETERS

	No RelMoCo	BC RelMoCo	Full RelMoCo	Reference
RCS	33.43 dB	42.13 dB	42.13 dB	42.13 dB
ISLR	-5.78 dB	-5.80 dB	-5.83 dB	-5.98 dB
$\delta_{az}$	30.76 cm	30.17 cm	30.18 cm	30.15 cm

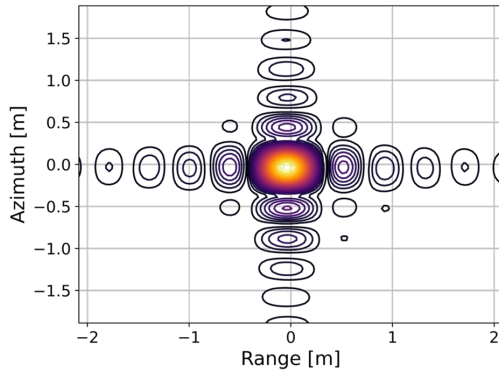


Fig. 17. Imaging result of the real point target for the reconstruction using the proposed full RelMoCo algorithm. The outermost contour level corresponds to a signal level of -29.13 dB relative to the peak.

data. However, before applying the decimation, the azimuth bandwidth of the system was reduced to 400.00 Hz by using a low pass filter (LPF). This step was needed to assure that there is no ambiguous signal outside the reconstruction's bandwidth of 450.00 Hz. Furthermore, the real data are modulated by the antenna pattern. The presented technique assumes that the antenna patterns of all channels are the same. As this was not the case, an additional processing was applied to compensate for inter-channel differences in the antenna patterns, however a detailed description is beyond the scope of the current study. The principle parameters used in this experiment are listed in Table VI.

To validate the previous simulation the same experiment was repeated using the real multi-channel airborne SAR data after the pre-processing steps mentioned before. Once again, the

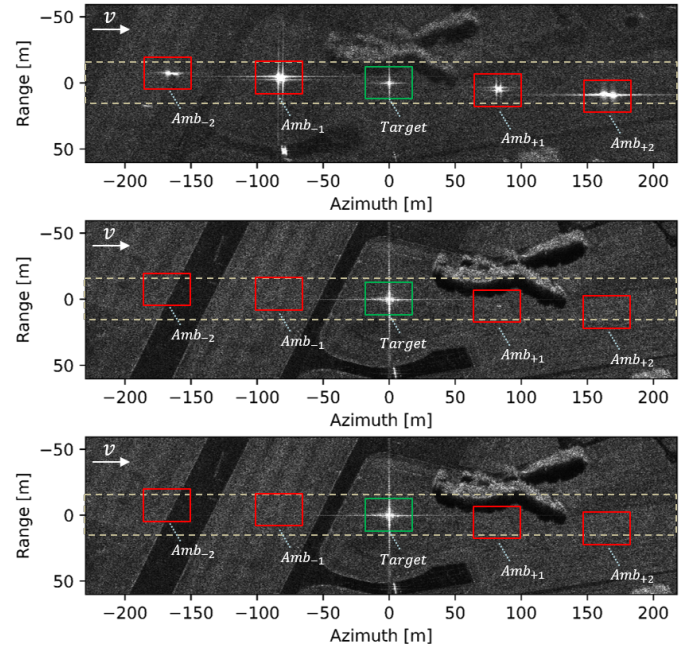


Fig. 18. Real reconstructed SAR images using different configurations for the algorithm. Reconstruction without any previous RelMoCo (top). Reconstruction applying the beam-center RelMoCo (middle). Reconstruction using both beam-center and Doppler-dependent RelMoCo (bottom). The red/green rectangles indicate the integration footprint used for the ambiguous/signal power to compute the AASR. The dotted square indicates the area in which the power of the range bins was integrated to obtain Fig. 19. The flight direction of the linear reference track after azimuth focusing is indicated on the upper left side of each image.

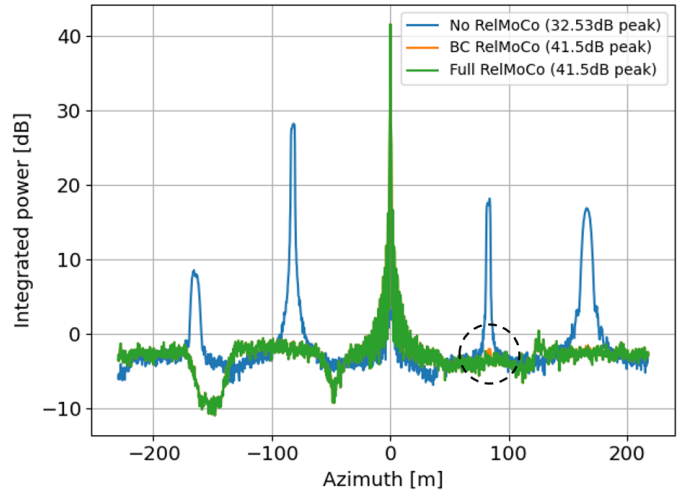


Fig. 19. Representation of the azimuth ambiguities after integrating the power of the range bins in the dotted area depicted in Fig. 18. The dotted circles highlight the residual azimuth ambiguity connected to an uncompensated Doppler-related phase error. The peak power of each reconstructed point target is shown in the legend.

subsampled data were reconstructed using the reconstruction algorithm without any RelMoCo, with only beam-center RelMoCo, and with the full RelMoCo. A flat DEM with the reference target height was utilized during the reconstruction. The focused reconstructed target using different configurations is shown in Fig. 18 and the AASR is presented in Table VII. The

oversampled real data could not be directly subsampled to have an equivalent PRF as the output of the reconstruction without applying an interpolation. For this reason, no ambiguity-free target was used to separate more accurately target integrated power from ambiguous power. Consequently, the ambiguous power was obtained by simply integrating the power in the areas of the original reconstructed focused image where the ambiguities were expected to be seen (red squares in Fig. 18). In Fig. 17 a zoom of the real reconstructed focused point target after using the full RelMoCo is depicted. As in the simulation, the azimuth resolution achieved was close to the nominal resolution of 0.3 m. Table VIII lists the other performance parameters introduced in Section IV-A. The values in Table VII are very close to the ones obtained in the simulation (see Table II), which validates the accuracy of the point target simulator used in Section IV-A. An interesting result is that the azimuth resolution obtained using the full RelMoCo technique was slightly worse than without introducing any residual Doppler-dependent RelMoCo step. Nevertheless, the difference is less than 1 mm, which is a small price for the sake of a better AASR.

The results obtained for the real data are consistent with the simulations carried out. In particular, the results of Fig. 18 are remarkably close to those of Fig. 11. In the case where no RelMoCo was utilized, the ambiguity suppression fails: One of the ambiguities has an integrated power higher than the integrated power of the target itself. The consequences are quite visible in the top plot in Fig. 18, where the clutter seems to be shifted related to the other plots. As in the previous sub-section, the reconstruction using just the beam-center RelMoCo already improved the ambiguity suppression considerably, but a first-order ambiguity ( $Amb_{+1}$ ) is still visible because of uncompensated Doppler residual phase errors. Finally, the plot at the bottom of Fig. 18 shows an ambiguity-free point target as we observed in the simulations, demonstrating the potential of the proposed reconstruction algorithm. As in the previous sub-section, the power of the range bins within the dotted area in Fig. 18 were integrated to obtain Fig. 19. In this plot it can be observed that the residual ambiguity present in the middle panel of Fig. 18 is almost at the same level as the clutter, showing that the performance of the beam-center RelMoCo was close to satisfactory. Comparing the peak powers (see legend in Fig. 19), the green-colored point target achieves a peak signal power 8.97 dB higher than the blue-colored point target, which is very similar to the simulation outcome. The local minima on the left side of the graph (orange and green lines in Fig. 19) correspond to the roads of the airport visible in Fig. 18.

## V. CONCLUSIONS AND FUTURE WORK

The work presented in this paper overcomes the detrimental impact of inter-channel motion inconsistencies in airborne DBF SAR systems using an azimuth reconstruction, where the PRF is lower than the recorded Doppler bandwidth. The reconstruction using the proposed RelMoCo technique achieved the desired azimuth ambiguity suppression, rendering the ambiguities invisible in the focused SAR image for both real and simulated data.

The RelMoCo technique introduces phase corrections that minimize mismatches between the multi-channel signal model and the data. In addition, the transformation of an original semi-active multi-channel SAR configuration into a fully-active constellation simplifies the bistatic IRF definition in airborne DBF SAR systems, such as the one presented in this investigation.

Extending the definition of the bistatic IRF to include residual Doppler-dependent phase errors has further improved the performance of the reconstruction in terms of azimuth ambiguity suppression. Separating the reconstruction filtering into two steps accounts for the polychromatic nature of SAR signals to perform a more accurate reconstruction. The division of the undersampled range-compressed SAR image into small azimuth blocks is introduced to minimize the impact of velocity variations. Results obtained from realistic simulated data confirm that this adaptive approach is necessary in practice. It also allows the implementation of parallelization to accelerate the processing at the cost of a slightly higher computational effort. Finally, further experiments have revealed that the algorithm is very sensitive to inaccuracies in the DEM, such that the use of an accurate elevation model to avoid a considerable degradation of the AASR becomes mandatory. The results of the reconstruction of real multi-channel airborne SAR undersampled data have proven the potential of the proposed reconstruction algorithm to suppress azimuth ambiguities in a scenario with irregular motion.

An interesting topic for future work concerns the robustness of the algorithm. For example, a further study might analyze the impact of non-uniform azimuth sampling on noise scaling, which is a well-known drawback in matrix inversion-based reconstructions [11]. Additionally, the study can be expanded to DBF systems using the azimuth reconstruction with different antenna patterns for each receiving channel, which would be representative also for a real spaceborne scenario.

## REFERENCES

- [1] N. Gebert, "Multi-Channel Azimuth Processing for High-Resolution Wide-Swath SAR Imaging," Ph.D. dissertation, Karlsruher Institut für Technologie, 2009.
- [2] P. Cheng, J. Wan, Q. Xin, Z. Wang, M. He, and Y. Nian, "An Improved Azimuth Reconstruction Method for Multichannel SAR Using Vandermonde Matrix," *IEEE Geoscience and Remote Sensing Letters*, vol. 14, no. 1, pp. 67–71, Jan. 2017.
- [3] A. Papoulis, "Generalized Sampling Expansion," *IEEE Transactions on Circuits and Systems*, vol. 24, no. 11, pp. 652–654, Nov. 1977.
- [4] J. Brown, "Multi-Channel Sampling of Low-Pass Signals," *IEEE Transactions on Circuits and Systems*, vol. 28, no. 2, pp. 101–106, Feb. 1981.
- [5] G. Krieger, N. Gebert, and A. Moreira, "Unambiguous SAR Signal Reconstruction from Nonuniform Displaced Phase Center Sampling," *IEEE Geoscience and Remote Sensing Letters*, vol. 1, no. 4, pp. 260–264, Oct. 2004.
- [6] D. Cerutti-Maori, J. Klare, I. Sikaneta, and C. Gierull, "Signal Reconstruction with Range Migration Correction for High-Resolution Wide-Swath SAR Systems," in *EUSAR 2014; 10th European Conference on Synthetic Aperture Radar*, 2014, pp. 1–4.
- [7] N. Sakar, M. Rodriguez-Cassola, P. Prats-Iraola, A. Reigber, and A. Moreira, "Analysis of Geometrical Approximations in Signal Reconstruction Methods for Multistatic SAR Constellations with Large Along-Track Baseline," *IEEE Geoscience and Remote Sensing Letters*, vol. 15, no. 6, pp. 892–896, Jun. 2018.
- [8] N. Sakar, M. Rodriguez-Cassola, P. Prats-Iraola, and A. Moreira, "Azimuth Reconstruction Algorithm for Multistatic SAR Formations with Large Along-Track Baselines," *IEEE Transactions on Geoscience and Remote Sensing*, vol. 58, no. 3, pp. 1931–1940, Mar. 2020.

- [9] N. Gebert, G. Krieger, and A. Moreira, "Digital Beamforming on Receive: Techniques and Optimization Strategies for High-Resolution Wide-Swath SAR Imaging," *IEEE Transactions on Aerospace and Electronic Systems*, vol. 45, no. 2, pp. 564–592, Apr. 2009.
- [10] M. Wang, W. Yu, R. Wang, L. Guo, and X. Luo, "Improved Azimuth Multichannel SAR Imaging for Configurations with Redundant Measurements," *IEEE Geoscience and Remote Sensing Letters*, vol. 12, no. 8, pp. 1610–1614, Aug. 2015.
- [11] B. Liu and Y. He, "Improved DBF Algorithm for Multichannel High-Resolution Wide-Swath SAR," *IEEE Transactions on Geoscience and Remote Sensing*, vol. 54, no. 2, pp. 1209–1225, Feb. 2016.
- [12] N. Liu, R. Wang, Y. Deng, S. Zhao, and X. Wang, "Modified Multichannel Reconstruction Method of SAR with Highly Nonuniform Spatial Sampling," *IEEE Journal of Selected Topics in Applied Earth Observations and Remote Sensing*, vol. 10, no. 2, pp. 617–627, Feb. 2017.
- [13] Z. Li, H. Wang, T. Su, and Z. Bao, "Generation of Wide-Swath and High-Resolution SAR Images from Multichannel Small Spaceborne SAR Systems," *IEEE Geoscience and Remote Sensing Letters*, vol. 2, no. 1, pp. 82–86, Jan. 2005.
- [14] I. Sikaneta, C. H. Gierull, and D. Cerutti-Maori, "Optimum Signal Processing for Multichannel SAR: With Application to High-Resolution Wide-Swath Imaging," *IEEE Transactions on Geoscience and Remote Sensing*, vol. 52, no. 10, pp. 6095–6109, Oct. 2014.
- [15] S.-X. Zhang, M.-D. Xing, X.-G. Xia, L. Zhang, R. Guo, Y. Liao, and Z. Bao, "Multichannel HRWS SAR Imaging Based on Range-Variant Channel Calibration and Multi-Doppler-Direction Restriction Ambiguity Suppression," *IEEE Transactions on Geoscience and Remote Sensing*, vol. 52, no. 7, pp. 4306–4327, Jul. 2014.
- [16] D. Cerutti-Maori, I. Sikaneta, J. Klare, and C. H. Gierull, "MIMO SAR Processing for Multichannel High-Resolution Wide-Swath Radars," *IEEE Transactions on Geoscience and Remote Sensing*, vol. 52, no. 8, pp. 5034–5055, Aug. 2014.
- [17] Y. Zhang, W. Wang, Y. Deng, and R. Wang, "Signal Reconstruction Algorithm for Azimuth Multichannel SAR System Based on a Multi-objective Optimization Model," *IEEE Transactions on Geoscience and Remote Sensing*, vol. 58, no. 6, pp. 3881–3893, Jun. 2020.
- [18] M. Suess, B. Grafmueller, and R. Zahn, "A Novel High Resolution, Wide Swath SAR System," in *IGARSS 2001. Scanning the Present and Resolving the Future. Proceedings. IEEE 2001 International Geoscience and Remote Sensing Symposium (Cat. No.01CH37217)*. IEEE, 2001.
- [19] N. Goodman, S. C. Lin, D. Rajakrishna, and J. Stiles, "Processing of Multiple-Receiver Spaceborne Arrays for Wide-Area SAR," *IEEE Transactions on Geoscience and Remote Sensing*, vol. 40, no. 4, pp. 841–852, Apr. 2002.
- [20] N. Sakar, M. Rodriguez-Cassola, P. Prats-Iraola, and A. Moreira, "Sampling Analysis and Processing Approach for Distributed SAR Constellations with Along-Track Baselines," *IEEE Transactions on Geoscience and Remote Sensing*, vol. 60, pp. 1–12, 2022.
- [21] M. Villano, G. Krieger, and A. Moreira, "Staggered SAR: High-Resolution Wide-Swath Imaging by Continuous PRI Variation," *IEEE Transactions on Geoscience and Remote Sensing*, vol. 52, no. 7, pp. 4462–4479, Jul. 2014.
- [22] N. Gebert, F. Q. de Almeida, and G. Krieger, "Airborne Demonstration of Multichannel SAR Imaging," *IEEE Geoscience and Remote Sensing Letters*, vol. 8, no. 5, pp. 963–967, Sep. 2011.
- [23] R. Wang, Y. Deng, P. Wang, and N. Wang, "Airborne X-Band SAR for Demonstrating Two-Dimensional Digital Beamforming," in *2017 IEEE International Geoscience and Remote Sensing Symposium (IGARSS)*, Jul. 2017, pp. 3841–3843, iSSN: 2153-7003.
- [24] A. Liu, F. Wang, H. Xu, and L. Li, "N-SAR: A New Multichannel Multimode Polarimetric Airborne SAR," *IEEE Journal of Selected Topics in Applied Earth Observations and Remote Sensing*, vol. 11, no. 9, pp. 3155–3166, Sep. 2018.
- [25] J. P. Navarro Castillo, R. Scheiber, M. Jaeger, and A. Moreira, "Multi-Channel SAR Image Reconstruction Using Data of DLR's New DBF-SAR Airborne System," in *EUSAR 2022; 14th European Conference on Synthetic Aperture Radar, 2022*, pp. 1–6.
- [26] A. Reigber, R. Scheiber, M. Jager, P. Prats-Iraola, I. Hajnsek, T. Jagdhuber, K. P. Papathanassiou, M. Nannini, E. Aguileria, S. Baumgartner, R. Horn, A. Nottensteiner, and A. Moreira, "Very-High-Resolution Airborne Synthetic Aperture Radar Imaging: Signal Processing and Applications," *Proceedings of the IEEE*, vol. 101, no. 3, pp. 759–783, Mar. 2013.
- [27] Z. Chen, Z. Zhang, J. Qiu, Y. Zhou, W. Wang, H. Fan, and R. Wang, "A Novel Motion Compensation Scheme for 2-D Multichannel SAR Systems with Quaternion Posture Calculation," *IEEE Transactions on Geoscience and Remote Sensing*, vol. 59, no. 11, pp. 9350–9360, Nov. 2021.
- [28] J. Chen, M. Xing, H. Yu, B. Liang, J. Peng, and G.-C. Sun, "Motion Compensation/Autofocus in Airborne Synthetic Aperture Radar: A Review," *IEEE Geoscience and Remote Sensing Magazine*, vol. 10, no. 1, pp. 185–206, Mar. 2022.
- [29] A. Moreira and Y. Huang, "Airborne SAR Processing of Highly Squinted Data Using a Chirp Scaling Approach with Integrated Motion Compensation," *IEEE Transactions on Geoscience and Remote Sensing*, vol. 32, no. 5, pp. 1029–1040, 1994.
- [30] A. Moreira, J. Mittermayer, and R. Scheiber, "Extended Chirp Scaling Algorithm for Air- and Spaceborne SAR Data Processing in Stripmap and ScanSAR Imaging Modes," *IEEE Transactions on Geoscience and Remote Sensing*, vol. 34, no. 5, pp. 1123–1136, Sep. 1996.
- [31] G. Fornaro, G. Franceschetti, and S. Perna, "On Center-Beam Approximation in SAR Motion Compensation," *IEEE Geoscience and Remote Sensing Letters*, vol. 3, no. 2, pp. 276–280, Apr. 2006.
- [32] P. Prats, K. A. Camara de Macedo, A. Reigber, R. Scheiber, and J. J. Mallorqui, "Comparison of Topography- and Aperture-Dependent Motion Compensation Algorithms for Airborne SAR," *IEEE Geoscience and Remote Sensing Letters*, vol. 4, no. 3, pp. 349–353, Jul. 2007.
- [33] K. de Macedo and R. Scheiber, "Precise Topography- and Aperture-Dependent Motion Compensation for Airborne SAR," *IEEE Geoscience and Remote Sensing Letters*, vol. 2, no. 2, pp. 172–176, Apr. 2005.
- [34] P. Prats, A. Reigber, and J. Mallorqui, "Topography-Dependent Motion Compensation for Repeat-Pass Interferometric SAR Systems," *IEEE Geoscience and Remote Sensing Letters*, vol. 2, no. 2, pp. 206–210, Apr. 2005.
- [35] R. Scheiber and V. Bothale, "Interferometric Multi-Look Techniques for SAR Data," in *IEEE International Geoscience and Remote Sensing Symposium*, vol. 1, Jun. 2002, pp. 173–175 vol.1.
- [36] V. Zamparelli, S. Perna, and G. Fornaro, "An Improved Topography and Aperture Dependent Motion Compensation Algorithm," in *2012 IEEE International Geoscience and Remote Sensing Symposium*, Jul. 2012, pp. 5805–5808, iSSN: 2153-7003.
- [37] Y.-l. Li, X.-d. Liang, C.-b. Ding, L.-j. Zhou, and Q. Ding, "Improvements to the Frequency Division-Based Subaperture Algorithm for Motion Compensation in Wide-Beam SAR," *IEEE Geoscience and Remote Sensing Letters*, vol. 10, no. 5, pp. 1219–1223, Sep. 2013.
- [38] R. Afroz, R. Scheiber, B. Ng, and D. Abbott, "Improved Subaperture Based Aperture-Dependent Motion Compensation Based on Adaptive Blocking and Apodization," in *2021 IEEE International Geoscience and Remote Sensing Symposium IGARSS*, Jul. 2021, pp. 3161–3164, iSSN: 2153-7003.
- [39] A. Ribalta, "One-Step Motion Compensation Algorithm for Squinted SAR," in *2016 IEEE International Geoscience and Remote Sensing Symposium (IGARSS)*, Jul. 2016, pp. 1154–1157, iSSN: 2153-7003.
- [40] R. Horn, A. Nottensteiner, A. Reigber, J. Fischer, and R. Scheiber, "F-SAR — DLR's New Multifrequency Polarimetric Airborne SAR," in *2009 IEEE International Geoscience and Remote Sensing Symposium*, vol. 2, Jul. 2009, pp. II-902–II-905, iSSN: 2153-7003.
- [41] A. Reigber, E. Schreiber, K. Trappschuh, S. Pasch, G. Müller, D. Kirchner, D. Geßwein, S. Schewe, A. Nottensteiner, M. Limbach, A. Schreiber, T. Rommel, R. Horn, M. Jäger, R. Scheiber, S. V. Baumgartner, S. K. Joshi, A. B. C. da Silva, and A. Moreira, "The High-Resolution Digital-Beamforming Airborne SAR System DBFSAR," *Remote Sensing*, vol. 12, no. 11, p. 1710, May 2020.
- [42] M. Jäger, R. Scheiber, and A. Reigber, "Robust, Model-Based External Calibration of Multi-Channel Airborne SAR Sensors Using Range Compressed Raw Data," *Remote Sensing*, vol. 11, no. 22, p. 2674, Nov. 2019.



**Juan Pablo Navarro Castillo** was born in Murcia, Spain, in 1994. He received the B.Sc. and M.Sc. degrees in Telecommunication Engineering from the Technical University of Cartagena (UPCT), Cartagena, Spain, in 2016 and 2018, respectively.

In 2017, he completed an internship at Elettronica GmbH, Bonn, Germany, where he worked on designing and testing RF chains for ground-based passive radar systems. From 2018 to 2021, he served as an RF Engineer and Technical Team Lead at AKKA Technologies, Ingolstadt, Germany, contributing to the development of antennas for Audi's automotive wireless communication systems. Since 2021, he has been with the German Aerospace Center (DLR), Microwave and Radar Institute, Oberpfaffenhofen, Germany, as a member of the Signal Processing Group within the Synthetic Aperture Radar (SAR) Technology Department, where he is currently pursuing a Ph.D. degree, focusing on digital beamforming techniques for SAR systems. His research interests include radar signal processing algorithms, digital beamforming, motion compensation, antenna pattern correction, and SAR image formation.



**Rolf Scheiber** received the Dipl.-Ing. (M.S.) degree in electrical engineering from the Technical University of Munich, Germany in 1994 and the Dr.-Ing. (PhD) degree in 2003 also in electrical engineering from the University of Karlsruhe, Germany with a thesis on airborne SAR interferometry.

Since 1994 he has been with the German Aerospace Center (DLR), Microwaves and Radar Institute, where he developed the first operational high precision interferometric SAR processor for its E-SAR airborne sensor. Since 2001 he is heading the Signal Processing Group within the SAR Technology Department, where he is supervising the DLR's F-SAR and DBFSAR airborne SAR processing activities. Dr. Scheiber supported several demonstrator projects for spaceborne SAR, among which the first demonstration of the TOPS imaging mode of Sentinel-1 with TerraSAR-X data and the development of the staring spotlight mode SAR processor for TerraSAR-X. He has authored or co-authored more than 40 peer-reviewed journal papers, more than 200 conference papers and holds 3 patents. His research interests include algorithm development for air- and spaceborne SAR focussing, motion compensation, SAR interferometry, DEM generation, differential SAR interferometry, SAR tomography, circular SAR as well as radio ice-sounding algorithms and applications.



**Marc Jäger** received the B.A. (Hons) degree in computer science from the University of Cambridge, U.K., and the M.Sc. degree (with distinction) in digital signal and image processing from DeMontfort University, Leicester, U.K.

He currently works at the German Aerospace Center (DLR), where his research is primarily concerned with the calibration and processing of polarimetric and interferometric multi-channel airborne synthetic aperture radar data. In addition, he is involved in the development of processing algorithms for tomographic imaging and digital beamforming.



**Alberto Moreira** (Fellow, IEEE) received the bachelor's and master's degrees in electrical engineering from the Aeronautical Technological Institute (ITA), São José dos Campos, in 1984 and 1986, respectively, and the PhD degree (Hons.) from the Technical University of Munich, Germany, in 1993. From 1996 to 2001, he was the Head of the Synthetic Aperture Radar (SAR) Technology Department, German Aerospace Center (DLR), Oberpfaffenhofen, Germany. Under his leadership, the DLR airborne SAR system has been upgraded to operate in innovative imaging modes like polarimetric SAR interferometry, tomography and holography.

Since 2001, Prof. Moreira is the Director of the Microwaves and Radar Institute at DLR and a Professor with the Karlsruhe Institute of Technology (KIT), in the field of microwave remote sensing. His DLR's Institute contributes to several scientific programs and projects for spaceborne SAR missions like TerraSAR-X, TanDEM-X, SAR-Lupe and SARah as well as Kompsat-6, PAZ, Sentinel-1, BIOMASS, ROSE-L, Harmony, Sentinel-1NG, Envison and VERITAS. The mission TanDEM-X, led by his Institute, has generated a global, high-resolution digital elevation model of the Earth with unprecedented accuracy. Prof. Moreira is the initiator and principal investigator (PI) for this mission. He has served as a member for the ESA Mission Advisory Groups of ENVISAT/ASAR, Sentinel-1, and Hydroterra, and most recently as a member of the Science Study Team for the ESA's EnVision mission. Prof. Moreira is author or co-author of more than 500 publications in international conferences and journals, 8 book chapters, and holds more than 45 international patent grants in the radar and antenna field. His professional interests and research areas encompass spaceborne radar end-to-end system design, microwave techniques and system concepts, signal processing, and remote sensing applications.

Prof. Moreira has served as President of the IEEE Geoscience and Remote Sensing Society (GRSS) in 2010 as well as General Co-Chair of IGARSS (2012) and General Chair of EUSAR (2006). He was founder and chair of the GRSS German Chapter (2003-2008), served as Associate Editor for the IEEE Geoscience and Remote Sensing Letters (2003-2007) and for the IEEE Transactions on Geoscience and Remote Sensing (since 2005), and is serving as chair of the Major Awards of GRSS since 2017. He and his colleagues received the GRSS Transactions Prize Paper Awards in 1997, 2001, and 2007 and the GRSS Letters Prize Paper Award in 2015 and 2017. He is also recipient of several international awards including the IEEE Aerospace and Electronic Systems Society (AESS) Fred Nathanson Award (1999), the IEEE Kiyoo Tomiyasu Technical Field Award (2007), IEEE W.R.G. Baker Award from the IEEE Board of Directors (2012), the IEEE GRSS Distinguished Achievement Award (2014), and the IEEE Dennis J. Picard Medal for Radar Technologies and Applications (2023).